Article

Molecular Cell

Impact of MicroRNA Levels, Target-Site Complementarity, and Cooperativity on Competing Endogenous RNA-Regulated Gene Expression

Graphical Abstract

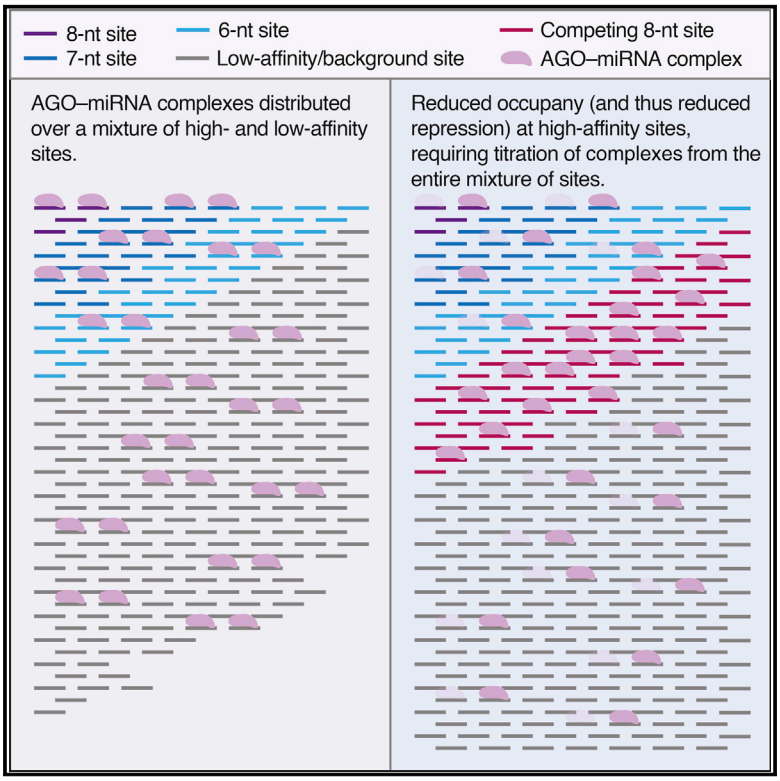

Authors

Rémy Denzler, Sean E. McGeary, Alexandra C. Title, Vikram Agarwal, David P. Bartel, Markus Stoffel

Correspondence

dbartel@wi.mit.edu (D.P.B.), stoffel@biol.ethz.ch (M.S.)

In Brief

Denzler et al. show that effects of competing miRNA sites are insensitive to reduced miRNA activity, low-affinity/background miRNA sites contribute to competition, and adjacent miRNA sites can cooperatively sequester miRNAs. Overall, their results reduce the prospects of observing an effect from a ceRNA.

Highlights

- ceRNA-mediated derepression is typically insensitive to reduced miRNA activity
- Extensively paired sites can reduce derepression thresholds by triggering miRNA decay
- Weak sites can contribute to target-site competition without imparting repression
- Closely spaced sites of the same or different miRNAs cooperatively sequester miRNAs

Accession Numbers

GSE76288

Denzler et al., 2016, Molecular Cell *64*, 565–579
November 3, 2016
http://dx.doi.org/10.1016/j.molcel.2016.09.027

Molecular Cell
Article

Impact of MicroRNA Levels, Target-Site Complementarity, and Cooperativity on Competing Endogenous RNA-Regulated Gene Expression

Rémy Denzler,[1] Sean E. McGeary,[2,3,4] Alexandra C. Title,[1] Vikram Agarwal,[2,3,4,5] David P. Bartel,[2,3,4,*] and Markus Stoffel[1,6,*]
[1]Institute of Molecular Health Sciences, Swiss Federal Institute of Technology in Zurich (ETH Zurich), Otto-Stern-Weg 7, 8093 Zürich, Switzerland
[2]Howard Hughes Medical Institute, Cambridge, MA 02142, USA
[3]Whitehead Institute for Biomedical Research, Cambridge, MA 02142, USA
[4]Department of Biology
[5]Computational and Systems Biology Program
Massachusetts Institute of Technology, Cambridge, MA 02139, USA
[6]Lead Contact
*Correspondence: dbartel@wi.mit.edu (D.P.B.), stoffel@biol.ethz.ch (M.S.)
http://dx.doi.org/10.1016/j.molcel.2016.09.027

SUMMARY

Expression changes of competing endogenous RNAs (ceRNAs) have been proposed to influence microRNA (miRNA) activity and thereby regulate other transcripts containing miRNA-binding sites. Here, we find that although miRNA levels define the extent of repression, they have little effect on the magnitude of the ceRNA expression change required to observe derepression. Canonical 6-nt sites, which typically mediate modest repression, can nonetheless compete for miRNA binding, with potency ~20% of that observed for canonical 8-nt sites. In aggregate, low-affinity/background sites also contribute to competition. Sites with extensive additional complementarity can appear as more potent, but only because they induce miRNA degradation. Cooperative binding of proximal sites for the same or different miRNAs does increase potency. These results provide quantitative insights into the stoichiometric relationship between miRNAs and target abundance, target-site spacing, and affinity requirements for ceRNA-mediated gene regulation, and the unusual circumstances in which ceRNA-mediated gene regulation might be observed.

INTRODUCTION

MicroRNA (miRNA) levels have long been known to influence the magnitude of target-gene repression (Bartel, 2009). More recent studies point out that the number of predicted binding sites present in the transcriptome also affects the activity of miRNAs (Arvey et al., 2010; Garcia et al., 2011). Consistent with this concept, strong overexpression of natural or artificial RNAs that contain miRNA sites can titrate miRNAs away from natural targets, thereby reducing the repression of these transcripts (Ebert et al., 2007; Franco-Zorrilla et al., 2007; Mukherji et al., 2011; Hansen et al., 2013; Memczak et al., 2013). These observations are extended by the notion that a site-containing transcript found naturally within cells can act as competing endogenous RNA (ceRNA) and regulate other site-containing transcripts by increasing or decreasing the miRNA activity (Poliseno et al., 2010; Cesana et al., 2011; Salmena et al., 2011; Karreth et al., 2015).

The ceRNA hypothesis remains controversial due to the lack of a plausible explanation for how modulating the expression of a single endogenous gene could perceptibly influence miRNA activity across all of its target sites. Two recent studies have empirically assessed the ceRNA hypothesis by quantifying the number of miRNA response elements (MREs) that must be added to detect ceRNA-mediated gene regulation (Bosson et al., 2014; Denzler et al., 2014). Both studies agree that determining the number of transcriptomic miRNA-binding sites is crucial for evaluating the potential for ceRNA regulation and that miRNA-binding sites are generally higher than the number of miRNA molecules. However, they differ in two aspects: (1) the experimental approaches used to determine the number of "effective" transcriptomic miRNA-binding sites and (2) the impact miRNA concentrations have on the number of binding sites that must be added to detect target gene derepression (derepression threshold [DRT]).

The discrepancies between these studies lead to different conclusions with respect to the likelihood of observing ceRNA effects in natural settings. The first study concluded that changes in ceRNAs must approach a miRNA's target abundance before they can exert a detectable effect on gene regulation (Denzler et al., 2014). Furthermore, because target abundance for a typical miRNA is very high, regulation of gene expression by ceRNAs is unlikely to occur in differentiated cells under physiological settings or most disease settings (Denzler et al., 2014). In addition, the study shows that the DRT remains constant when miRNA activity is reduced. A subsequent review presents a mathematical model that assesses binding-site occupancy and competition at different assumed target abundances (Jens and

Rajewsky, 2015). This in silico model predicts that only global and collective changes in binding sites can produce an effect on target abundance large enough to detectably derepress target genes, which concurs with the results and conclusions of Denzler et al. (2014).

The second study presents a "hierarchical affinity model," in which the miRNA abundance is proposed to determine the respective susceptibility to ceRNA-mediated regulation (Bosson et al., 2014). In this model, the suggestion is that, as miRNA concentration increases and Ago-miRNA complexes spread to weaker and weaker sites (with affinity inferred from the site hierarchy of 8-nt > 7-nt > 6-nt site), the effective target-site abundance grows too large for physiological ranges of ceRNA expression to influence repression. By this reasoning, physiological ceRNA changes can nevertheless influence repression by a more modestly expressed miRNA, with its correspondingly lower effective target-site abundance. Moreover, the use of high-throughput cross-linking to detect targets leads to lower target-abundance estimates, which further increases the plausibility of ceRNA regulation (Bosson et al., 2014). However, experimental support for the proposed influence of miRNA concentration is correlative and lacks direct experimental evidence, such as manipulation of miRNA activity and measurement of resulting DRT changes.

Denzler et al. (2014) propose that sites of all different affinities contribute to the effective target abundance, regardless of the miRNA concentration. Here, we call the model of Denzler et al. (2014) the "mixed-affinity model" to distinguish it from the hierarchical affinity model. The mixed-affinity model recognizes that a high-affinity site will contribute more to effective target-site abundance than a low-affinity site (Denzler et al., 2014). However, in aggregate, low-affinity sites, because of their high numbers within the transcriptome, still make a substantial contribution to the effective target-site abundance for each miRNA—even for more modestly expressed miRNAs.

Other studies suggest that the ceRNA crosstalk of two transcripts is stronger and more specific when they share a large number of sites to different miRNA seed families. This hypothesis emerged from observations in cancer models, in which the expression of a particular oncogene correlates with its pseudogene, and both transcripts share a high sequence homology in their 3′ UTRs and are reported to co-regulate each other through a ceRNA mechanism (Poliseno et al., 2010; Karreth et al., 2015). Even if transcripts containing multiple sites can exert an additive effect of independently acting binding sites, sites for each miRNA family would still have to individually reach the high thresholds necessary to observe target-gene derepression. Therefore the simple presence of multiple binding sites alone would not be expected to be sufficient to increase the likelihood of a ceRNA effect, unless the sites acted through a cooperative mechanism. Although the effect of cooperativity has been studied in the context of target-gene repression (Doench et al., 2003; Grimson et al., 2007; Saetrom et al., 2007; Broderick et al., 2011), it is unclear whether closely spaced miRNA-binding sites can sequester miRNA in a non-independent manner and hence increase the prospects of a ceRNA effect.

In this study, we examine the impact that miRNA levels have on the DRT and thereby address a key difference between the hierarchical affinity and mixed-affinity models. We then analyze the influence of target-site complementarity on ceRNA-mediated gene regulation and examine the extent to which closely spaced miRNA-binding sites can cooperatively influence the potency of target-gene derepression. Finally, we develop a mathematical model, which incorporates both the mixed-affinity binding and the repressive activities of miRNAs to recapitulate our results.

RESULTS

miR-294 Is Susceptible to Competition Despite High Expression Levels

A powerful tool for studying competition among MREs is a single-cell reporter assay that transcribes *mCherry* mRNA (with or without MREs in its 3′ UTR) and enhanced yellow fluorescent protein (*eYFP*) mRNA as an internal measure of reporter transcription (Mukherji et al., 2011; Bosson et al., 2014). Using analytical flow cytometry, *mCherry* reporter readout can be assessed over a broad range of added MREs. At high expression levels, MREs can compete with each other for miRNA binding, thereby causing derepression. Using this assay in embryonic stem cells (ESCs), some miRNAs need fewer competing MREs to mediate reporter derepression and are therefore more susceptible to ceRNAs than other miRNAs (Bosson et al., 2014).

To explore these different susceptibilities, we created reporter constructs for six highly expressed ESC miRNAs (miR-294, -293, -92, -16, -26, and -292-5p) (Bosson et al., 2014), containing zero (0s), or three (3s) 8-nt miRNA sites in the 3′ UTR of *mCherry* (Figure 1A). For the miRNA families miR-294, -293, and -92, reporters containing a single (1s) miRNA-binding site were also created. Sites for miR-294, -293, -92, and -16 (Figures 1B and 1C), but not those for miR-26 and -292-5p (data not shown) caused detectable miRNA-mediated repression of mCherry. The extent of repression of reporters for miR-294, -293, and -92 resembled that observed previously, as did the derepression of mCherry constructs harboring sites for miR-293 or miR-92 (Bosson et al., 2014). However, the 3s reporter construct for miR-294, a miRNA reported to be insensitive to competitor perturbations (Bosson et al., 2014), and the reporter for miR-16 were derepressed when eYFP fluorescence exceeded 2.2×10^4 or 2.8×10^4, respectively (Figure 1B). The ability to observe derepression of the miR-294 reporter presumably resulted from improvements to the equipment and protocol that enabled more precise measurements, as indicated by the improved SEM values, although differences between the ESCs might have also played a role. These results showing derepression of the mCherry reporter at similar competitor levels for both miR-294 and miR-16, two miRNAs present at very different levels in ESCs, and with very different miRNA:target ratios estimated by Bosson et al. (2014), support the mixed-affinity model.

Derepression of Target mRNAs Occurs at a High Threshold of Added Target Sites

The competition among MREs for miRNA binding is expected to occur not only between the added MREs within the *mCherry* mRNA but also between the added MREs and those of the

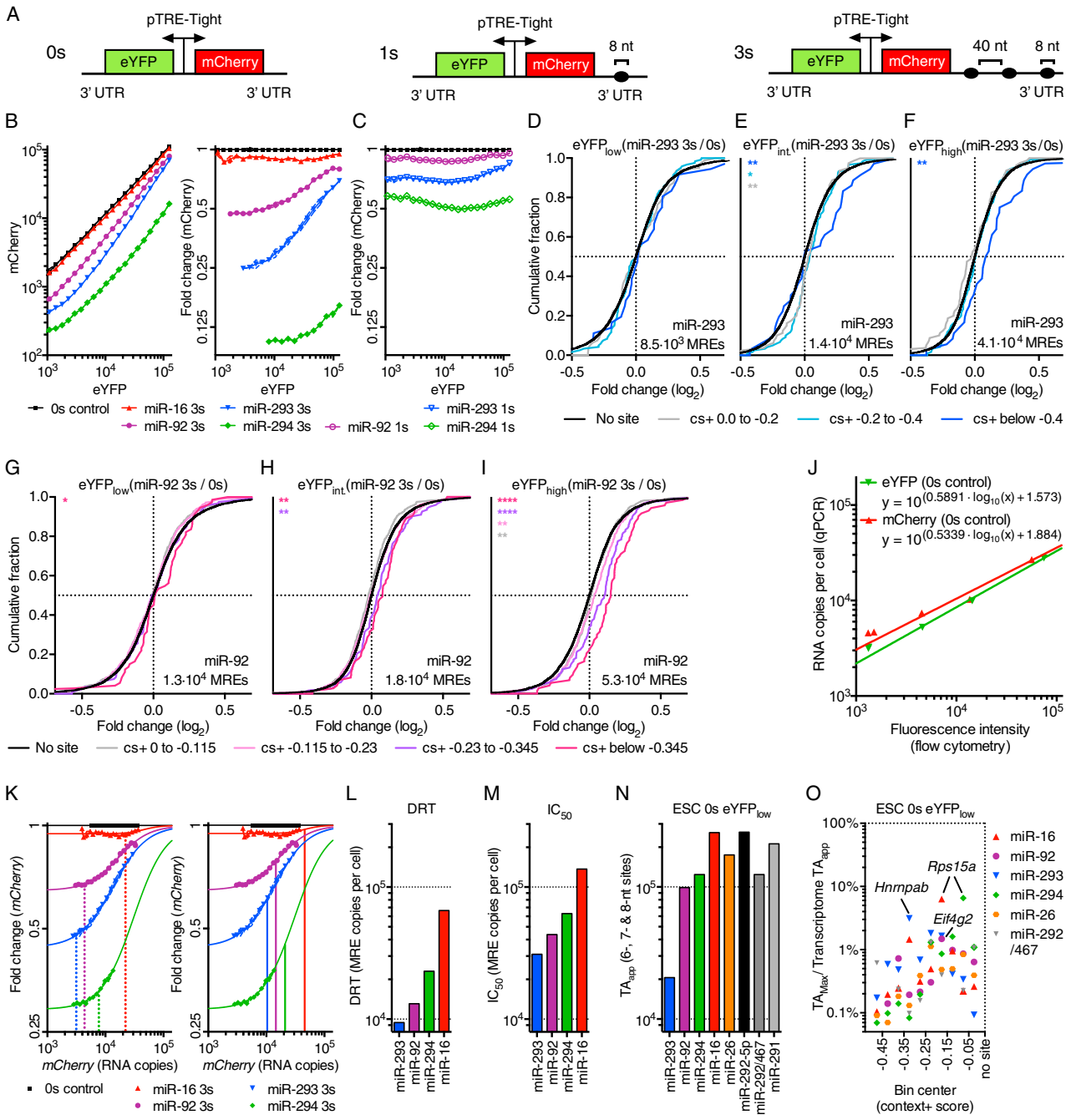

Figure 1. Derepression of Target mRNAs Occurs at a High Threshold of Added Target Sites

(A) Dual-color fluorescent reporter constructs containing zero (0s), one (1s), or three (3s) 8-nt miRNA site(s) in the 3′ UTR of *mCherry*.

(B and C) ESCs transfected with either a 3s (B), 1s (C), or 0s reporter construct (n = 3) with miRNA-binding sites for miR-294, -293, -92, or -16. Mean mCherry fluorescence (B, left), and mCherry fluorescence normalized to the 0s control (B, right and C) across 20 bins of eYFP.

(D–I) RNA-seq results (n = 2) of sorted ESCs shown in Figure S1A. ESCs were transfected with a 3s reporter for miR-293 (D–F) or miR-92 (G–I), or a 0s control, and gated for cells with low ($eYFP_{low}$) (D and G), intermediate ($eYFP_{int.}$) (E and H), or high eYFP ($eYFP_{high}$) (F and I) expression. Cumulative distribution function (CDF) of mRNA changes for predicted target genes with the indicated context+ score (cs+) bins (color) or for genes with no miRNA site (black). *mCherry* MREs per cell evaluated by qPCR are shown on each graph. *p < 0.05, **p < 0.01, ***p < 0.001, ****p < 0.0001, one-sided Kolmogorov-Smirnov (K-S) test. Also see Figures S1B and S1C.

(J) Relationship between reporter protein fluorescence measured by flow cytometry and RNA copies per cell evaluated by qPCR of ESCs transfected with the 0s reporter and sorted into four different bins of eYFP-expressing cells. Line represents non-linear regression of data points; respective equations are shown.

(legend continued on next page)

endogenous targets. To examine the effect on endogenous targets, ESCs transfected with the 0s or a 3s reporter for either miR-293 or miR-92 were sorted into three bins based on their eYFP expression (Figure S1A, available online). RNA sequencing (RNA-seq) of each bin revealed the number of MREs added per cell as well as differences in endogenous mRNA levels for cells with the 3s reporter compared to those with the 0s reporter. Endogenous mRNAs with predicted MREs were grouped based on the strength of their predicted response to the miRNA, as scored by the context+ model of TargetScan 6.2 (Garcia et al., 2011). For the middle, but not the lower, bin (1.4×10^4 and 0.85×10^4 added miR-293 MREs per cell, respectively), endogenous miR-293 targets were derepressed, as indicated by the significant shift in the distribution of mRNA fold-change values of the top predicted miR-293 targets (Figures 1D–1F and S1D–S1F; Table S1). Likewise, convincing miR-92 target derepression was not observed until exceeding 1.3×10^4 added miR-92 MREs (Figures 1G–1I and S1G–S1I).

Comparison of mCherry and eYFP fluorescence with the corresponding transcript copy numbers, as measured by qRT-PCR (qPCR), revealed that fluorescence and mRNA abundance were highly correlated, although the relationship was not one-to-one (Figure 1J). Because protein fluorescence intensity is an indirect readout that is not directly relevant to the competition that occurs on the level of mRNA and miRNA, we transformed the fluorescence values measured by flow cytometry in Figure 1B to transcript copies per cell by employing the standard curves of Figure 1J (Figures 1K and S1J). Strikingly, the DRT observed for miR-293 and miR-92 reporters (0.9×10^4 and 1.3×10^4 sites per cell, respectively; Figures 1K and 1L) resembled those observed by RNA-seq for endogenous targets, thereby validating the reporter output (after transforming fluorescence to transcript copy number) for endogenous target derepression.

We next calculated the number of MREs that must be added per cell to observe half-maximal derepression (termed half-maximal inhibitory concentration, or IC_{50}) of the different reporter constructs (Figures 1K and 1M). The number of miRNA molecules per ESC is reported to be 5.7×10^4 for miR-294, 2.6×10^3 for miR-293, 1.7×10^3 for miR-92, and 1.8×10^3 for miR-16 (Bosson et al., 2014), which was consistent with the relative levels of these miRNAs in our ESCs, as determined by small-RNA-seq (Figure S1L; Table S2). Thus, as observed for miR-122 in hepatocytes (Denzler et al., 2014), the IC_{50} values exceeded the number of miRNA molecules per ESC. In such a regime, the IC_{50} provides an empirical measure of the effective endogenous target-site abundance, as half-maximal derepression should be achieved when the competing sites reach an effective concentration matching that of the endogenous sites (Denzler et al., 2014).

In hepatocytes, the miR-122 IC_{50} (4.5×10^5 sites per cell) happens to correspond to the sum of all 3′ UTR 6-, 7-, and 8-nt sites of the transcriptome, leading to the idea that this sum, defined as the TA_{app}, can provide an estimate of the effective target-site abundance for other miRNAs (Denzler et al., 2014). To test this idea, we examined the correspondence between the newly determined IC_{50} values and the TA_{app} values for the ESC transcriptome. When comparing RNA-seq data with absolute copy numbers of *mCherry*, *eYFP*, and three differently expressed genes, a linear association was observed (Figure S1K), which provided a standard curve to transform RNA-seq data to absolute mRNA copies per cell, enabling TA_{app} values for eight active ESC miRNAs to be determined (Figure 1N). For all four miRNAs with IC_{50} values, the TA_{app} approached the IC_{50}, ranging from ~2-fold above the IC_{50} (miR-16, -92, and -294), to 1.5-fold below the IC_{50} (miR-293). Because TA values estimated from cross-linking (Bosson et al., 2014) strongly correlated with TA_{app} values (Figures S1M and S1N), but were ~7-fold lower, the cross-linking immunoprecipitation (CLIP)-estimated TA values were not more informative for the purposes of estimating the effective target-site abundance. We conclude that summing of 3′ UTR 6-, 7-, and 8-nt sites in the transcriptome provides a reasonable approximation of effective abundance of endogenous target sites.

The DRTs ranged between 12% (miR-92) and 30% (miR-293) of TA_{app}. Importantly, no endogenous transcript contributed such a large percentage to transcriptome TA_{app} of the ESC miRNAs examined. The largest contributor was ribosomal protein S15A (*Rps15a*) mRNA, which contributed 6.5% of the TA_{app} for both miR-294 and miR-16 (Figure 1O). Thus in ESCs, as in hepatocytes (Denzler et al., 2014), ceRNA-regulated gene expression through upregulation or downregulation of a single transcript is unlikely. Similar results have been reported in HEK293 cells (Yuan et al., 2015).

Derepression Threshold Values Are Insensitive to Changes in miRNA Activity

A key difference between the mixed-affinity and the hierarchical affinity models is the impact that miRNA levels have on the threshold required to detect derepression of target genes (Bosson et al., 2014; Denzler et al., 2014). To investigate this issue, we examined the influence that reduced miRNA activity has on the DRT in the single-cell assay. ESCs were transfected with either 0s or 3s miR-293 reporters, in addition to different concentrations of Antagomir-293 (Ant-293). Reduction of mCherry repression correlated with increasing Ant-293 concentrations, confirming that miR-293 activity was reduced in Antagomir-treated ESCs (Figure 2A). As observed for miR-122 in hepatocytes (Denzler et al., 2014), the DRTs and IC_{50} values did not decrease as miR-293 activity was reduced in ESCs (Figures 2B and S2A–S2C).

(K) Protein fluorescence values shown in (B) transformed to RNA copies per cell using the equations shown in (J). Vertical lines represent the DRT (dotted lines) or IC_{50} (solid lines).

(L and M) Bar plot of DRT (L) and IC_{50} (M) shown in (K).

(N) Transcriptome TA_{app} of ESCs transfected with the 0s reporter and sorted for low eYFP-expressing cells (ESC 0 s $eYFP_{low}$).

(O) Fractional contribution of the largest potential contributors to transcriptome TA_{app} of ESC 0s $eYFP_{low}$. Potential contributors were binned by their context+ score, and the top potential contributors are plotted within each bin.

Data represent mean ± SEM for (B), (C), and (K).

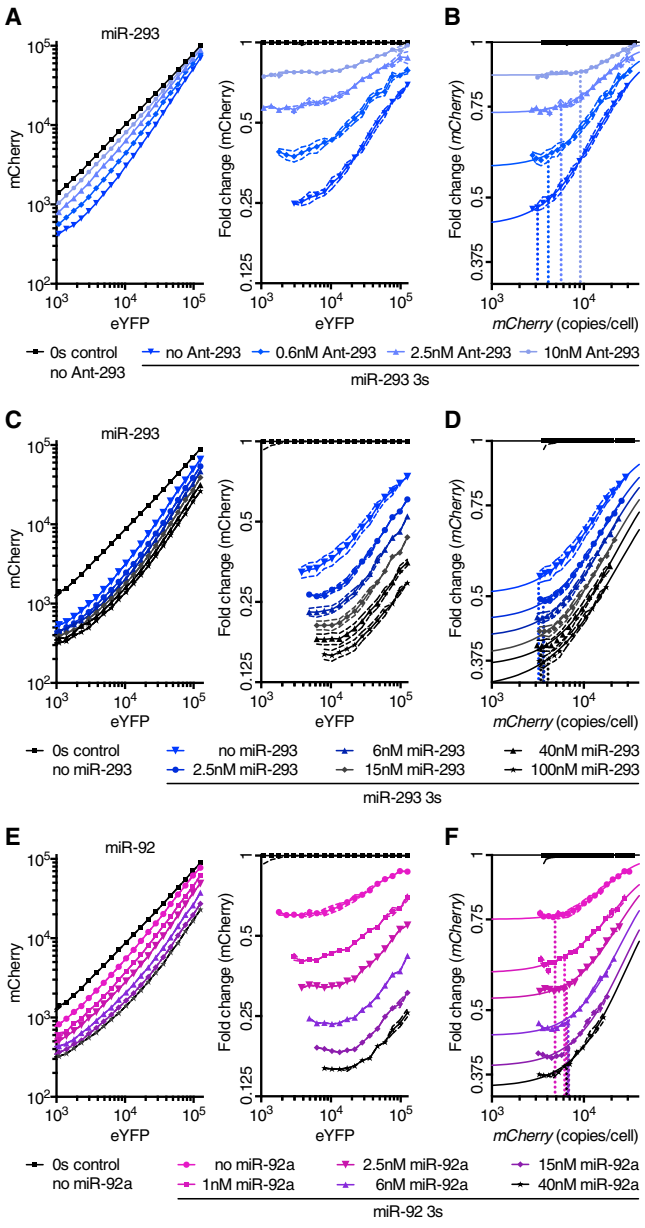

Figure 2. Derepression Threshold Values Are Insensitive to Changes in miRNA Activity

(A–F) ESCs co-transfected with a 3s reporter for miR-293 (A–D), miR-92 (E and F), or respective 0s reporter control, and different concentrations of Ant-293 (n = 3) (A and B), miR-293 (n = 6) (C and D), or miR-92 (n = 6) (E and F).

(A, C, and E) Mean mCherry fluorescence (left), and mCherry fluorescence normalized to the 0s control (right) across 20 bins of eYFP.

(B, D, and F) Protein fluorescence values shown in (A), (C), and (E) were transformed to RNA copies per cell using the equations shown in Figure 1J. Vertical, dotted lines denote the DRT.

Data represent mean ± SEM for all panels.

We next increased miRNA activity and examined the effect on the DRT. ESCs were transfected with the dual-fluorescent reporter and different concentrations of miRNA duplex. When quantified with respect to eYFP fluorescence or *eYFP* mRNA copies, we detected an increase in the DRT as more miRNA was transfected (Figures 2C, 2E, S2D, S2E, S2G, and S2H). However, eYFP, unlike mCherry, is not a good measure for MRE induction as it is not repressed by the miRNA and hence does not inform how many MREs are actually expressed in a cell. Indeed, when quantified with respect to *mCherry* transcript abundance, the DRT of competing transcripts remained constant as more miRNA was transfected (Figures 2D, 2F, S2F, and S2I). These results monitoring DRTs after decreasing or increasing miRNA activities supported the mixed-affinity model, in which less abundant miRNAs should be no more susceptible to ceRNA effects than are more abundant miRNAs (Denzler et al., 2014).

Extensively Paired Sites Are More Potent Than 8-nt Sites and Trigger miRNA Decay

We investigated whether the DRT was also insensitive to increased miRNA levels in primary hepatocytes. A 4-fold increase in miR-122, attained by infecting hepatocytes with a recombinant adenovirus expressing the miR-122 precursor (Ad-miR-122), resulted in decreased levels of endogenous miR-122 target mRNAs (Figures S3A–S3C). To manipulate miR-122 MREs and measure the subsequent effects on miR-122 target genes, we increased the levels of the miR-122 target *AldolaseA* (*AldoA*) mRNA using an adenovirus (Ad-AldoA) that carried either a mutated site (Mut), one (1s), or three sites (3s) to miR-122 (Figure 3A). Hepatocytes were infected at different multiplicities of infection (MOIs), at either basal or elevated miR-122 levels (Figures 3B and S3D–S3G). At endogenous miR-122 levels, we began to observe miR-122 target derepression when more than 2.1×10^5 miR-122 MREs were introduced (Figure 3C). The DRT did not increase when endogenous miR-122 levels were raised 4-fold (Figure 3C), which is in agreement with our observations in ESCs. Of note, the higher DRT observed in hepatocytes compared to ESCs is expected based on the larger cytoplasm and number of mRNAs per cell in hepatocytes.

Our finding that derepression occurred at only high thresholds of added target sites seemed to disagree with a study in HeLa cells that used "bulged" binding sites with near-perfect complementarity (Mukherji et al., 2011). We sought to test the possibility that sites with perfect complementarity to the miRNA 3′ region might yield different results because they mediate miRNA degradation. Hepatocytes were infected with Ad-AldoA containing either a mutated or a bulged (bu4) binding site (Figure 3A). Interestingly, derepression was already observed when exceeding only 5×10^4 bulged miR-122 MREs per cell (Figures 3D, 3E, S3H, and S3I), confirming that bulged sites are more efficient than 8-nt sites in influencing miRNA activity. The efficiency of target-mRNA derepression mediated by bulged sites correlated well with a decrease of miR-122, but not miR-16, levels (Figures 3F and S3J), suggesting that derepression was induced by enhanced miRNA degradation rather than direct competition between miRNA-binding sites.

Target-mediated miRNA decay is associated with tailing and trimming of the miRNA (Ameres et al., 2010). Indeed, we observed reduced miR-122 signal with evidence of tailing and trimming when bulged, but not 8-nt, seed matches caused target-gene derepression (Figures 3G and S3K). These results

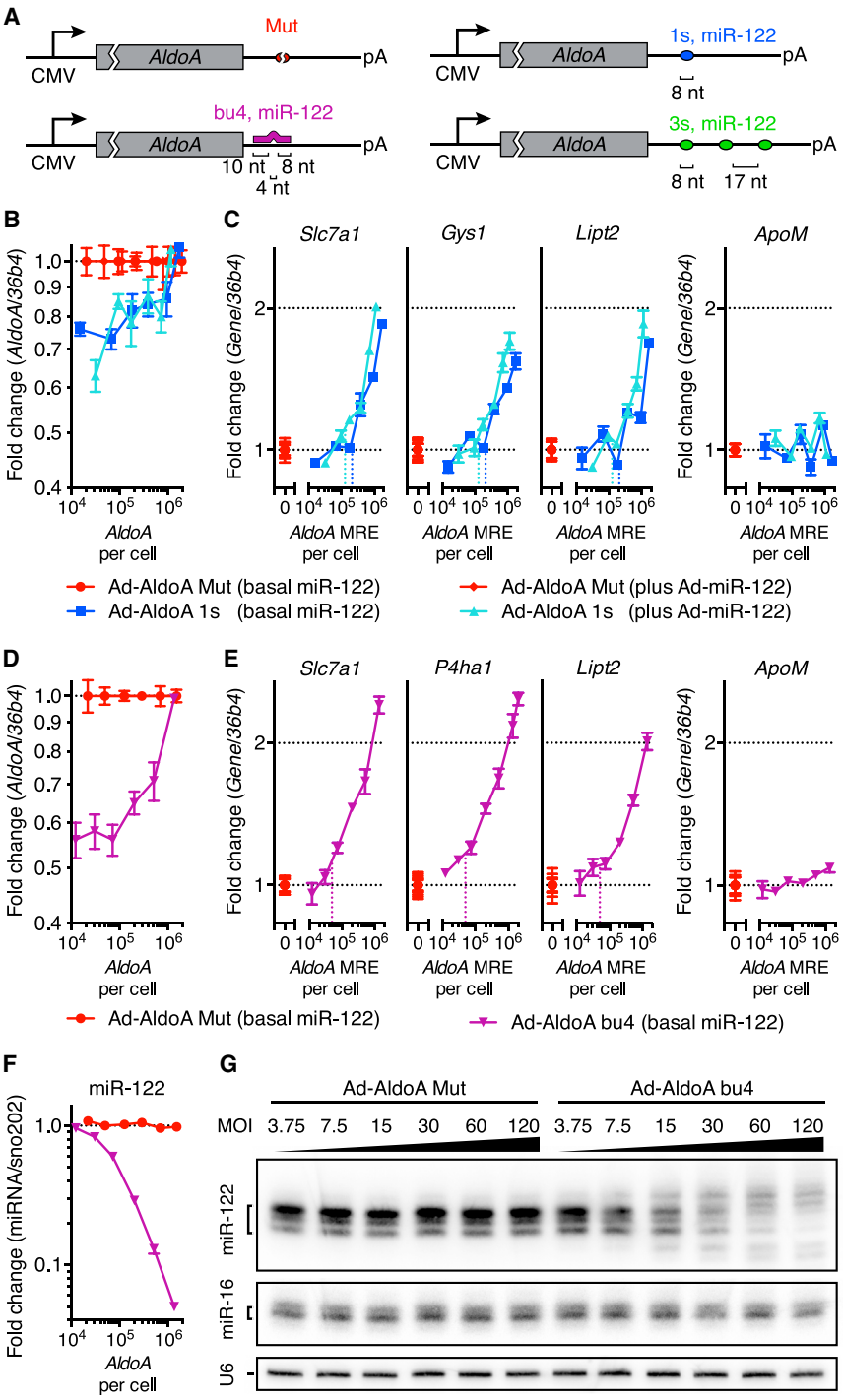

Figure 3. Extensively Paired Sites Are More Potent Than 8-nt Sites and Trigger miRNA Decay

(A) Schematic overview of the different *AldoA*-expressing adenovirus constructs.

(B–G) Primary hepatocytes (n = 4) infected with different MOIs of Ad-AldoA 1s (B and C), bu4 (D–G), or respective Ad-AldoA Mut controls at either basal miR-122 levels (B–G) or with co-infected Ad-miR-122 (B and C). Relative levels of *AldoA* (B and D), miR-122 target genes and control non-target gene (*ApoM*) (C and E), or miR-122 (F). Vertical, dotted lines denote the DRT. miRNA levels are relative to the lowest MOI of Ad-AldoA Mut at basal miR-122 levels. (G) Northern blot analysis of miR-122, miR-16, and U6 at basal miR-122 levels.

Data represent mean ± SEM for all panels. Also see Figure S7.

confirmed that bulged sites with perfect complementarity to the miR-122 3′ region reduce miRNA activity primarily through miRNA degradation rather than competition with other binding sites. Therefore, to be effective, these bulged sites need not approach the effective abundance of the miRNA target sites, but need only to be sufficiently abundant that the amount of target-mediated RNA decay substantially decreases the miRNA abundance.

miRNA Target Derepression for let-7, miR-194, and miR-192 Also Occurs at a High Threshold of Added MREs

To consider the susceptibility of other hepatocyte miRNAs to ceRNA-mediated gene regulation, we first measured absolute levels of miR-122 and six other miRNA seed families highly expressed in liver (Denzler et al., 2014). These levels ranged from 3.8×10^3 to 1.4×10^5 copies per cell (Figures 4A and S4A) and correlated well with small-RNA-seq data (Figure S4B; Table S2). We selected four families (let-7, miR-194, -192, and -101) that were not influenced by control virus expression (Figure S4C) and were expressed above 1.8×10^4 copies per cell. To study the sensitivity of these four miRNA families to competing RNA perturbations, Ad-AldoA constructs were generated in which the miR-122 site was replaced with a single 8-nt site (1s) for the respective miRNA (Figure 4B). We first infected hepatocytes with different MOIs of Ad-AldoA Mut or 1 s (let-7). Derepression of let-7 targets, which were validated by transfection of let-7f mimics (Figures S4D–S4G), was observed when >2.1×10^5 let-7 MREs were expressed per cell (Figures 4C, S4H, and S4I). This DRT was consistent with RNA-seq results (Figures 4D–4F and S4J–S4L; Table S3). In contrast, addition of up to 10^6 MREs of either miR-192, miR-194, or miR-101 through respective Ad-AldoA infections did not result in detectable derepression of validated targets (Figures S4M–S4P; data not shown), suggesting that the endogenous level of 1.8×10^5 miRNA molecules per cell did not impart sufficient repression upon which derepression could act. We therefore performed the analogous

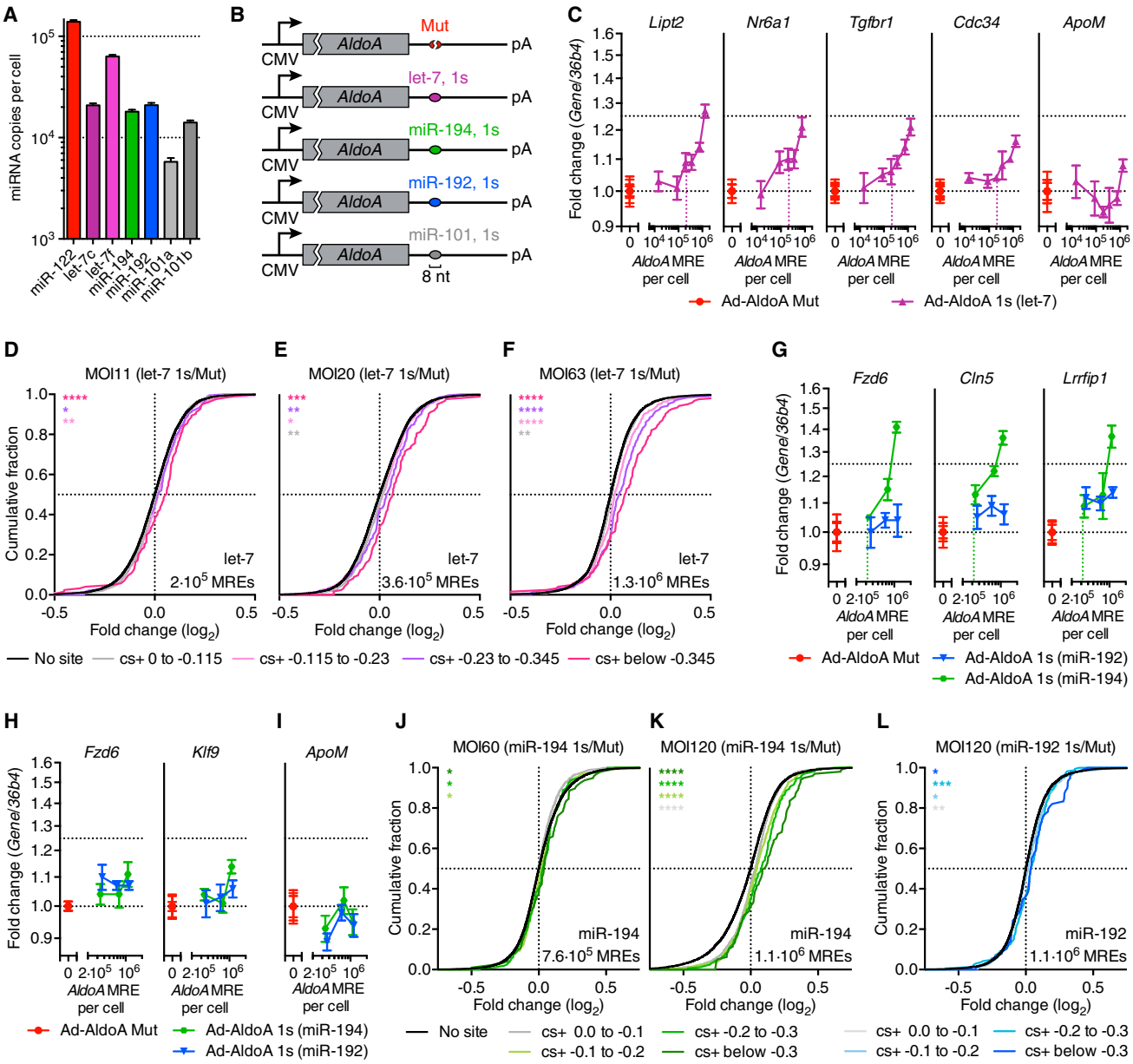

Figure 4. miRNA Target Derepression for let-7, miR-194, and miR-192 Also Occurs at a High Threshold of Added MREs

(A) Absolute copies per cell of hepatocyte miRNAs.

(B) Schematic overview of Ad-AldoA constructs harboring a mutated site (Mut), or one (1s) 8-nt binding site for let-7, miR-194, -192, or -101.

(C–F) Primary hepatocytes infected with different MOIs of Ad-AldoA Mut or 1s (let-7).

(C) Relative expression of let-7 target genes and control non-target gene (*ApoM*).

(D–F) CDF of RNA-seq data (n = 2) showing mRNA changes for predicted target genes of let-7 with the indicated cs+ bins (color) or for transcripts with no miRNA site (black).

(G–L) Hepatocytes infected with different MOIs of Ad-AldoA Mut, 1s (miR-192), or 1s (miR-194), in addition to MOI 15 Ad-miR-192/194. Relative levels of miR-194 (G) or miR-192 (H) target genes, and control non-target gene (*ApoM*) (I). CDF of RNA-seq data (n = 2) showing mRNA changes for predicted target genes of miR-194 (J and K) or miR-192 (L) with the indicated cs+ bins (color) or for genes with no miRNA site (black).

AldoA MREs per cell evaluated by qPCR are shown on each graph. *p < 0.05, **p < 0.01, ***p < 0.001, ****p < 0.0001, one-sided K-S test. Vertical, dotted lines denote the DRT.

Data represent mean ± SEM (n = 4) for all panels.

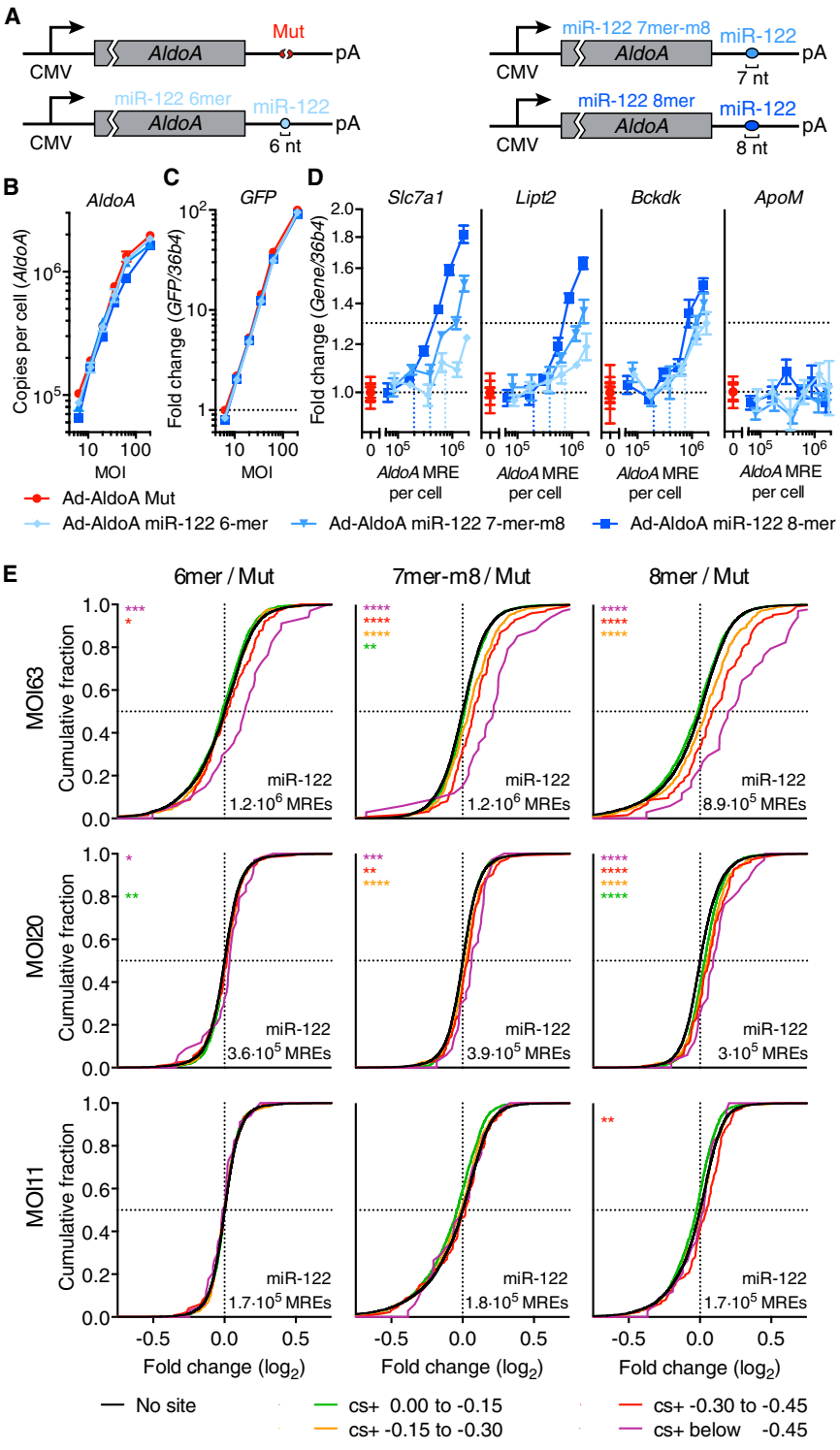

Figure 5. The 6-, 7-, and 8-nt Sites Contribute Comparably to Target Abundance of miR-122

(A) Schematic overview of Ad-AldoA constructs used in this figure.

(B–E) Primary hepatocytes infected with different MOIs of Ad-AldoA miR-122 8-mer, miR-122 7-mer-m8, miR-122 6-mer, or Mut. Absolute copy numbers per cell of *AldoA* (B), relative gene expression of *GFP* (C), and of miR-122 target genes or control non-target gene (*ApoM*) (D). (E) CDF of RNA-seq data (n = 2) showing mRNA changes for predicted target genes of miR-122 with the indicated cs+ bins (color) or for genes with no respective miRNA site (black). *AldoA* MREs per cell evaluated by qPCR are shown on each graph. *p < 0.05, **p < 0.01, ***p < 0.001, ****p < 0.0001, one-sided K-S test. See also Figures S5C and S5D.

Vertical, dotted lines denote the DRT. Data represent mean ± SEM (n = 4) for all panels.

experiment under conditions of elevated miR-192 and miR-194 levels using recombinant adenovirus expression (Ad-miR-192/194) (Figure S4M). Increasing miR-194 by 4.5-fold increased repression to a level at which target derepression could be observed, with a DRT of >3.2 × 10^5 added miR-194 MREs per cell (Figures 4G, 4I, S4Q, and S4R). RNA-seq analysis confirmed a similar DRT for predicted miR-194 targets (Figures 4J, 4K, S4S, and S4T). Because repression of predicted targets was not readily observed when increasing miR-192 levels by 3.7-fold (Figure S4O), derepression was also difficult to measure (Figures 4H, 4I, S4Q, and S4R), although some signal for derepression was detected when 1.1 × 10^6 miR-192 MREs were added (Figures 4L and S4U). Together, these results indicated that derepression of let-7, miR-192, and miR-194 targets in hepatocytes occurred at similar or higher DRTs than previously observed for miR-122 targets.

The 6-, 7-, and 8-nt Sites Contribute Comparably to Target Abundance

The different levels of repression efficacy and preferential conservation observed for 6-, 7-, and 8-nt site types (Bartel, 2009) raised the question as to the extent to which these site types differ in their efficacy as competitors. Accordingly, we infected hepatocytes with different MOIs of Ad-AldoA constructs harboring either a mutated or one 6-, 7-, or 8-nt site to miR-122 (Figure 5A). Derepression of miR-122 targets was observed when adding each of the three site types, with a clear relationship between competitor site type and DRT (Figures 5B–5D). This relationship, in which DRT increased as site size decreased, was also observed when extending our analysis to the transcriptome (Figures 5E and S5A). For example, the derepression observed for the 6-nt site at MOI 63 was between that

observed for the 8-nt site at MOI 11 and 20, suggesting that as a competitor it was about 20% as effective as the 8-nt site. With respect to the 7-nt site, derepression at MOI 63 exceeded that observed for the 8-nt site at MOI 20, and derepression at MOI 20 surpassed that measured for the 8-nt site at MOI 11, suggesting that as a competitor the 7-nt site was about 50% as effective as the 8-nt site. Employing these factors to calculate a weighted TA_{app} only decreased the TA_{app}, without affecting the relative ranking of the respective miRNA TA_{app} (Figure S5B). These results indicate that, in aggregate, 7-nt sites, which are 3- to 8-fold more abundant than 8-nt sites, contribute more to effective target-site abundance than do 8-nt sites, and that 6-nt sites contribute more to effective target-site abundance than might have been expected from their marginal efficacy in target repression.

Derepression Is Enhanced When Mediated by Closely Spaced MREs

Although the cooperative effect of closely spaced miRNA-binding sites has been studied in the context of mRNA repression (Doench et al., 2003; Grimson et al., 2007; Saetrom et al., 2007; Broderick et al., 2011), the role of cooperatively spaced miRNA-binding sites has not been investigated in the setting of site competition. We therefore analyzed whether closely spaced miRNA-binding sites can cooperatively sequester miRNA molecules and hence reduce the number of sites required for derepression.

Cooperatively acting MREs within endogenous 3′ UTRs tend to be between 8 and ~60 nt apart (Grimson et al., 2007; Saetrom et al., 2007). We thus generated Ad-AldoA constructs harboring one 8-nt site for miR-122 and one for let-7, separated by 58 nt (Ad-AldoA 2x +58nt), or respective single-site controls (Figure 6A), and infected hepatocytes at different MOIs. Interestingly, predicted let-7 targets that lacked miR-122 sites showed stronger derepression when let-7 MREs were added through constructs harboring a nearby miR-122 site (Figures 6B–6D, S6A, and S6B). Analogous results were obtained for the derepression of miR-122 targets by miR-122 MREs that had an adjacent let-7 site, showing that competition for binding to one miRNA family can be influenced by a nearby site of a different family. To achieve the same level of derepression conferred by isolated sites, the sites with nearby cooperative sites required only 20%–50% as many molecules per cell (Figure 6B).

To study the influence that the spacing of the miR-122 and let-7 sites has on the ability to cause cooperative competition, we infected hepatocytes with various MOIs of differently spaced Ad-AldoA 2x constructs (Figure 6A). Although the cooperative effect of Ad-AldoA-2x-mediated gene regulation persisted independently of whether the let-7–binding site was 58 nt upstream or downstream of the miR-122 site—indicating that a specific intervening sequence or structure was not required—no cooperative effect was observed when the two sites were 255 or 997 nt apart (Figures 6E–6G, S6C, and S6D). When changing the 8-nt miR-122 site on Ad-AldoA 2x +58nt to a 7- or 6-nt site (Figure 6A), a strong relationship was observed between site type and the magnitude of the cooperative effect (Figures 6H, 6I, and S6E–S6G). Moreover, at the transcriptome level, predicted let-7 targets that lacked predicted miR-122 sites were significantly more derepressed if the competing let-7 site had an adjacent miR-122 site (Figures 6J and S6H), thereby confirming that closely spaced binding sites of co-expressed miRNAs can boost the efficacy of competing sites.

We then investigated whether the DRT was lower in conditions in which cooperativity was present by infecting hepatocytes with different MOIs using Ad-AldoA miR-122, let-7, and 2x +58nt. Derepression of miR-122 and let-7 target genes was detected when 7×10^4 *AldoA* copies of the 2x +58nt construct were exceeded (Figures 6K–6N, S6I, and S6J). Depending on whether binding sites of either miR-122 or let-7 alone, or both together are included in the cooperative DRT, the 7×10^4 *AldoA* copies would correspond to a DRT of either 7 or 14×10^4 MREs, which is either 3.1- or 1.5-fold lower (let-7), or 2.2- or 1.1-fold lower (miR-122), respectively, than the previously determined DRTs. Regardless of the DRT interpretation, these results indicate that the cooperative action of sites can detectibly boost the prospects of ceRNA-mediated gene derepression.

Mathematical Framework for the Mixed-Affinity Model

Mathematical simulations of miRNA-target interactions have been used to evaluate the potential effects of competing MREs (Mukherji et al., 2011; Ala et al., 2013; Bosson et al., 2014; Jens and Rajewsky, 2015; Schmiedel et al., 2015). However, these simulations either model only the extent to which different site types are occupied by a miRNA without modeling repressive effects that are needed for comparison to experimental results (Bosson et al., 2014; Jens and Rajewsky, 2015), or they model the repression of mRNA from one or two genes without modeling competition of sites from other expressed transcripts (Mukherji et al., 2011; Ala et al., 2013; Schmiedel et al., 2015). These latter simulations also omit the bound form of the mRNA from its simulated abundance. Most importantly, previous simulations also ignore the influence of the large number of low-affinity, non-canonical/background sites.

We therefore built a mathematical framework that incorporates site-type occupancy, mRNA destabilization, and the range of binding-site affinities intrinsic to the mixed-affinity model. This framework was used to predict the influence of both target-site abundance and miRNA level on target derepression. As with previous simulations (Mukherji et al., 2011; Bosson et al., 2014; Jens and Rajewsky, 2015), we assumed that (1) molecular species are well mixed within the cytosol and their concentrations are not influenced by cell growth and division; (2) each mRNA and miRNA is produced at a constant rate, and unbound mRNAs and miRNAs undergo constant first-order decay; (3) upon association with a miRNA, the mRNA degradation rate increases, regardless of the site type; and (4) miRNA binding is reversible, and upon miRNA dissociation the mRNA degradation rate reverts to its original value. We also assumed that the Michaelis constant (K_M) describing mRNA degradation with respect to the miRNA-mRNA complex is well approximated by the complex dissociation constant (K_D), and that both bound and unbound mRNA are translated.

We first simulated the results of adding the 1s reporter for miR-293 to ESCs, as done in Figure 1C, setting levels of miR-293 and its canonical 3′ UTR sites to those measured by sequencing. Binding affinities of 6-, 7-, and 8-nt sites were

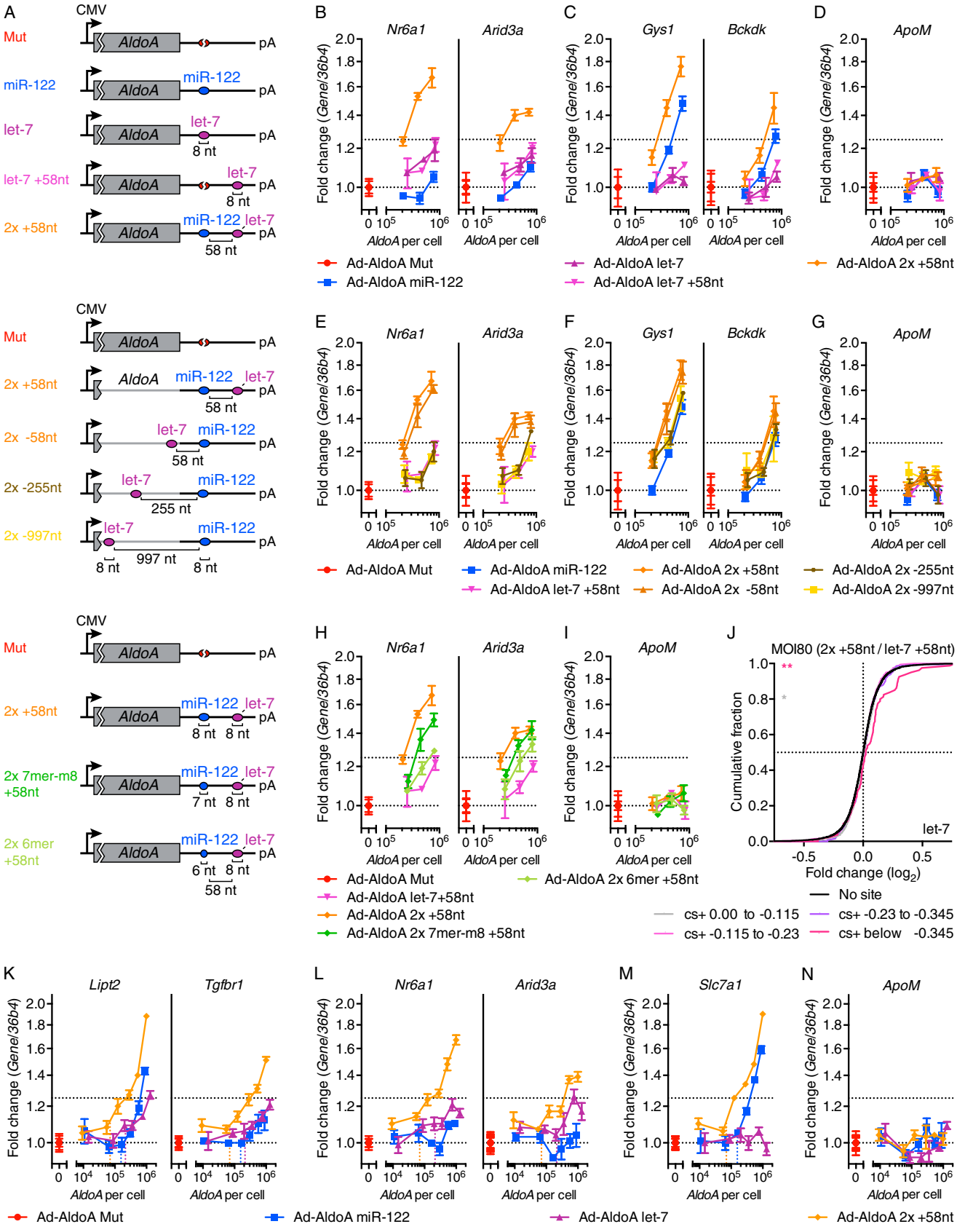

(legend on next page)

modeled with distributions centering on their measured affinities, and a distribution of low-affinity sites was added such that the simulated IC_{50} reflected the experimentally determined value of $\sim 3 \times 10^4$ copies per cell (Figure 7A). With this target-site distribution (Figure 7A, right), the simulation recapitulated other features of our results. For example, DRT values were only marginally sensitive to 10-fold changes in miRNA (Figure 7A, left), and this sensitivity seemed greater when plotted as a function of *eYFP*, the co-expressed mRNA lacking a miR-293 site (Figure 7A, middle). Moreover, the *mCherry* IC_{50} values were even less sensitive to miRNA changes (Figure 7A, left) and corresponded to the half-maximal occupancy values (Figure 7B).

Plotting the competition in terms of site occupancy (Figure 7B) allowed comparison to previous simulations that do not consider mRNA repression. Reconstructing the simulation of miR-293 binding in ESCs from Bosson et al. (2014), using their values for site affinity and abundance, showed that sensitivity to additional 8-nt sites was much greater than that observed in our experiments, as was the influence of miRNA levels on half-occupancy values (Figure 7C, left). Similar results were observed when applying the model of Jens and Rajewsky (2015), which uses the same mathematical framework as Bosson et al. (2014) but a continuous distribution of canonical site affinities (Figure 7C, right). Remarkably, after adding low-affinity sites such that the half-maximal occupancy value matched that inferred from our experimental results, both of the previous frameworks behaved indistinguishably from ours (Figures 7B and 7D). Thus, the fundamental difference between the mixed-affinity model and the other models, which enables our simulation to better match the experimental results, is the greater effective target abundance that results from consideration of many low-affinity sites.

DISCUSSION

Our results support the mixed-affinity model for miRNA site competition. In agreement with this model, we found that DRTs did not correlate with endogenous miRNA abundance and changed only modestly with experimental manipulations that increased or decreased miRNA levels. Because reducing miRNA levels does not substantially reduce the very high number of added MREs that are necessary to impart detectable derepression, changes in ceRNAs are not more likely to influence targets of miRNAs expressed at lower levels. Thus, the previous conclusion that a ceRNA effect on miR-122 targets in hepatocytes is unlikely to occur in normal physiological or disease conditions (Denzler et al., 2014) can now be more confidently extended to targets of other miRNAs in other cell types. Indeed, using two different cell types, testing several different miRNA families, and employing complementary single-transcript and high-throughput methods, we found that competing sites must approach ~10%–40% of a miRNA's TA_{app} in order to detectably influence miRNA activity. As nearly all transcripts each contribute <5% to TA_{app}, ceRNA-mediated gene regulation is very unlikely to occur under normal homeostatic conditions.

In disfavoring the hierarchical affinity model for site competition, we are not questioning the biochemical fact that some sites have more affinity than others, and thus low- and high-affinity sites exhibit differential occupancy. Indeed, although we disfavor the hierarchical affinity model with respect to site competition, it is nonetheless useful for explaining miRNA-mediated repression: when a miRNA is lowly expressed, only the highest-affinity sites are sufficiently occupied to mediate repression, but as miRNA expression increases, more and more intermediate- and low-affinity sites have occupancies sufficient to mediate repression. This model for repression is consistent with conclusions from cross-linking studies as well as those from mRNA-profiling studies showing a strong signal for derepression at 6-nt sites after loss of very highly expressed miRNAs (Giraldez et al., 2006; Bosson et al., 2014). The difference between modeling repression and modeling competition is that weak sites (including 6-nt, non-canonical, and background sites) all compete for binding even if they impart marginal or negligible repression and, importantly, this competition occurs regardless of the miRNA level. Although occupancy at any individual weak site is low, it cannot be discounted when modeling competition because weak, low-occupancy sites are in vast excess over high-affinity sites. The idea that these weak sites make a substantial contribution to effective target abundance is supported by our mathematical modeling showing that experimental results cannot be accurately simulated without considering the aggregate contribution of low-affinity sites. Also supporting this idea are single-molecule results showing that 6-nt sites and even some sites with only partial seed matches associate with the miRNA silencing complex at rates resembling those of the higher-affinity sites (Chandradoss et al., 2015; Salomon et al., 2015). Thus, even a miRNA expressed at a very low level, such as one molecule per cell, is expected to sample very many weak sites before (and after) occupying a high-affinity site.

Although miRNA levels do not affect the DRT, miRNA levels are important insomuch as they define the magnitude at which targets are initially repressed and hence the magnitude of effect that could theoretically be observed upon changes in ceRNA expression. Thus, ceRNA-regulated gene expression is

Figure 6. Derepression Is Enhanced When Mediated by Closely Spaced MREs

(A) Schematic overview of Ad-AldoA constructs used in this figure.

(B–J) Primary hepatocytes infected with different MOIs of Ad-AldoA constructs shown in (A). Relative gene expression of let-7 target genes (B, E, and H), miR-122 target genes (C and F), or control non-target gene (*ApoM*) (D, G, and I). (J) CDF of RNA-seq results (n = 2) showing mRNA changes from hepatocytes infected with MOI 80 of Ad-AldoA let-7 +58nt or 2x +58nt for predicted target genes of let-7 (with no predicted target sites for miR-122) with the indicated cs+ bins (color) or for genes with no let-7 or miR-122 miRNA sites (black). *p < 0.05, **p < 0.01, ***p < 0.001, ****p < 0.0001, one-sided K-S test.

(K–N) Hepatocytes infected with different MOIs of Ad-AldoA Mut, miR-122, let-7, or 2x +58nt. Relative gene expression of predicted target genes for both let-7 and miR-122 (K), let-7 target genes (L), a miR-122 target gene (M), or a control non-target gene (*ApoM*) (N). Vertical, dotted lines denote the DRT.

Data represent mean ± SEM (n = 4) for all panels.

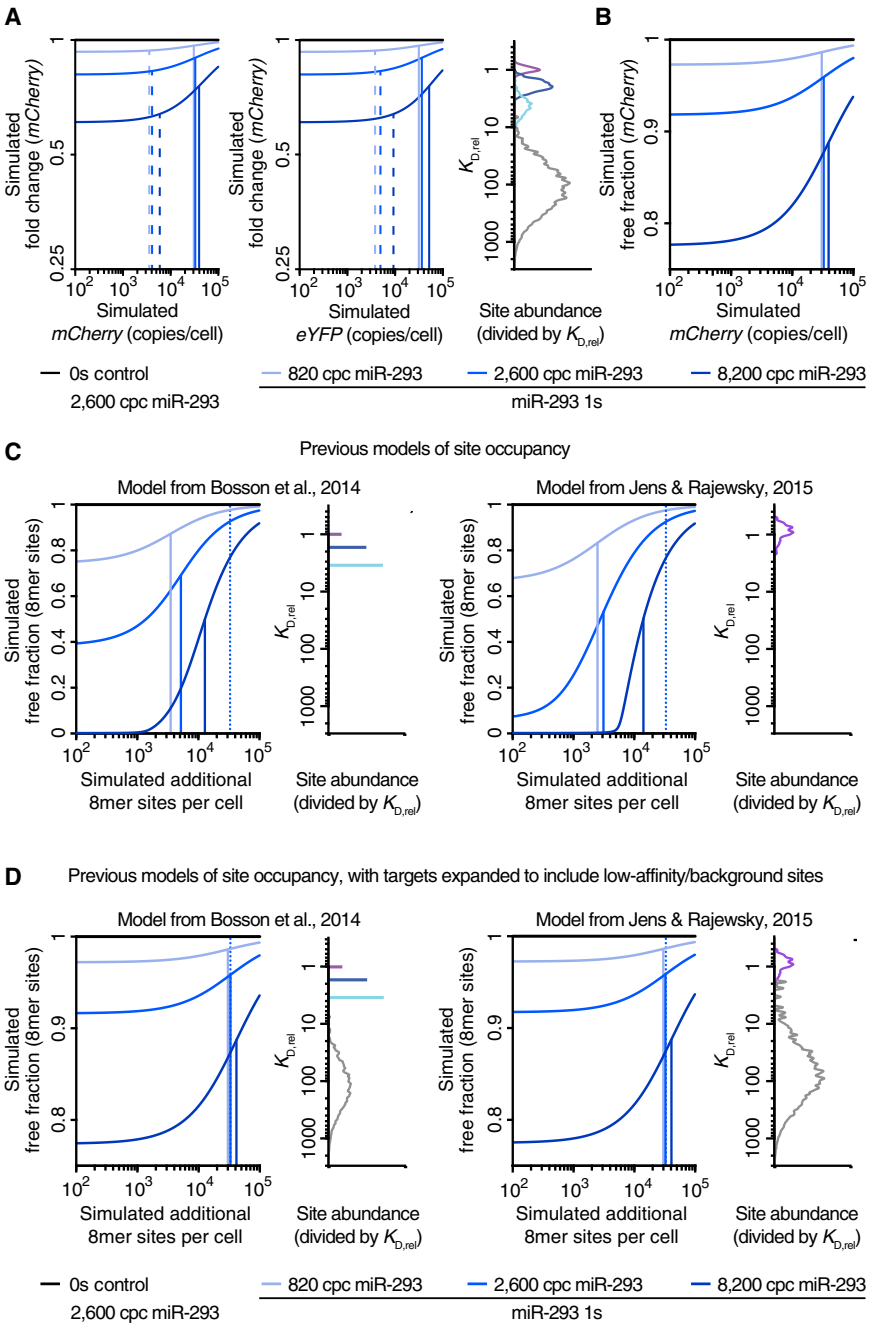

Figure 7. Mathematical Simulation of the Mixed-Affinity Model

(A) Simulated effects of changing miR-293 concentrations in ESCs on 8-nt target site repression (as performed in Figure 2), using the mathematical framework of the mixed-affinity model. Simulated *mCherry* fold-changes of the 1s reporter normalized to the 0s control are either plotted against *mCherry* (left) or *eYFP* (middle), indicating the IC_{50} (solid lines) and DRT (dashed lines), for each of the three simulated miR-293 levels (in copies per cell [cpc]). Also plotted is the binding affinity distribution of all simulated target sites (right), with the K_D of each site normalized to that of an 8-nt site and the abundance of each site scaled by its normalized K_D. Abundance of 8-, 7-, and 6-nt, and low-affinity sites for miR-293 are plotted separately (purple, blue, cyan, and gray, respectively). The abundance of the canonical sites was determined by sequencing and that of the low-affinity sites was set such that the IC_{50} matched that observed in Figure 1C.

(B) Site occupancy for the simulations in (A). Plotted is the simulated free fraction of *mCherry* 1s reporter as a function of its expression, otherwise as in (A).

(C) Simulated effects of changing miR-293 concentrations in ESCs on 8-nt target site occupancy using the mathematical models of site competition from Bosson et al. (2014) (left) or Jens and Rajewsky (2015) (right). Simulated free fraction of an added 8-nt target site is plotted as a function of its expression as in (B), using the binding-affinity distributions of the simulated target sites of the original studies, plotted as in (A). The IC_{50} inferred from Figure 1C is indicated (dotted lines).

(D) Simulations using the models of (C) but adding low-affinity sites to alleviate the discrepancy between the simulated and experimental results, otherwise as in (C).

expected to be more easily observed and more biologically relevant when miRNA levels are high.

When we conclude that miRNA levels do not substantially influence the DRT, we refer to the DRT as the number of sites that were measured in steady-state conditions in the presence of miRNA-mediated repression, such as those represented by the *mCherry* transcripts in the dual-fluorescence reporter system. In this system, it was important to account for the miRNA-mediated degradation of the competitor, as our conclusions would have differed if we determined the competitor concentration in the absence of miRNA repression, represented by the output of the co-transcribed eYFP reporter.

Bulged and fully complementary sites were the first site types to be investigated in the context of regulating miRNA activity through competition (Ebert et al., 2007; Franco-Zorrilla et al., 2007), and they have been widely used to inhibit or measure miRNA activity (Doench et al., 2003; Broderick et al., 2011; Mukherji et al., 2011; Mullokandov et al., 2012; Xie et al., 2012). However, these sites with extensive complementarity to the 3′ region of the miRNA can trigger degradation of the miRNA (Ameres et al., 2010). Indeed, we observed target-directed miRNA degradation in hepatocytes when adding bulged sites of miR-122. Hence, bulged sites can reduce miRNA activity predominantly through triggering miRNA degradation rather than by competing with other miRNA-binding sites. Likewise, endogenous transcripts with highly complementary binding sites might affect miRNA activity through degradation rather than competition, especially in situations of low or intermediate

miRNA levels, with this degradation mechanism requiring much lower expression levels to be consequential. For example, potent target-directed degradation has been described in primary neurons (de la Mata et al., 2015), and a highly complementary binding site has been identified in the linc-MD1 long non-coding RNA and implicated in muscle differentiation through a ceRNA mechanism (Cesana et al., 2011). Whether this complementary site can induce miRNA degradation or whether other such sites exist remains to be shown.

We found that 7-nt sites were 50% as effective as 8-nt sites in contributing to target abundance, and 6-nt sites were 20% as effective. This 20% efficacy compared to 8-nt sites was much greater than might have been expected from the marginal repression typically imparted by 6-nt sites, again illustrating how competition efficacy imperfectly mirrors repression efficacy. Because miRNA association rates (k_{on} values) of 6-, 7-, or 8-nt sites are similar (Chandradoss et al., 2015; Salomon et al., 2015), the difference between competition and repression presumably relates to the different dissociation rates (k_{off} values) of these site types. Perhaps, before any repression can begin, some time is required to remodel the target transcript, assembling TNRC6 (trinucleotide repeat containing 6) and the deadenylation complexes, such that the dwell time of the miRNA on 6-nt sites only rarely exceeds this lag time. Similar models have been proposed to explain the poor repression efficacy of sites in the path of the ribosome (Grimson et al., 2007) and inefficacy of non-canonical sites in 3′ UTRs, despite the compelling CLIP evidence for binding to the ineffective sites (Agarwal et al., 2015). In this way, site types that are marginal or ineffective with respect to repression can nonetheless contribute meaningfully to effective target-site abundance. Indeed, our mathematical simulations illustrate that, in aggregate, low-affinity, non-canonical/background sites contribute more to the effective target-site abundance than do the canonical sites.

As the sum of 6-, 7-, and 8-nt sites in transcriptome 3′ UTRs, TA_{app} is a crude approximation of the effective target site abundance, in that it overcounts effects of 6- and 7-nt 3′ UTR sites and misses both the sites outside of 3′ UTRs and the weak but highly abundant non-canonical sites in 3′ UTRs. Nonetheless, summing up all 6-, 7-, or 8-nt 3′ UTR sites equally without weighting approximated IC_{50} within a few fold, presumably because overcounting the effects of some sites largely offset the failure to count other sites.

Our competition results provided mechanistic insight into the cooperative effect sometimes observed for adjacent sites. Whereas two distantly spaced 3′ UTR sites typically confer the repression expected from their independent action, two more closely spaced sites often confer more repression than expected from independent action (Grimson et al., 2007; Saetrom et al., 2007). Previous studies of this phenomenon using repression as the output do not distinguish between cooperative binding of the two sites or some other type of cooperative function in repression. Our use of competition as the output, with the observation that transcripts containing two miRNA-binding sites spaced 58 nt apart cooperatively sequester miRNAs corresponding to each site, uniquely shows that cooperative binding occurs.

Although the mechanism of this cooperative binding is unknown, an attractive hypothesis is that nearby Argonaute proteins might be tethered to each other through binding of the same TNRC6 molecule, also known as glycine-tryptophan protein of 182 kDa (GW182) in flies (Huntzinger and Izaurralde, 2011; Fabian and Sonenberg, 2012). TNRC6 contains multiple Argonaute-binding sites that might simultaneously interact with multiple miRNA-loaded Argonaute proteins (Schirle and MacRae, 2012; Pfaff et al., 2013), thereby enabling adjacent transcript-bound Argonaute proteins to prolong the dwell times of each other.

In the previous study of miR-122 site competition in hepatocytes, the three-site construct appears only 3-fold more effective than the one-site construct, as would be expected for non-cooperative, independent action of the three sites (Denzler et al., 2014). Suspecting that cooperativity was not observed in this context because the number of different MOIs examined was insufficient to detect subtle differences, we revisited potential cooperative binding of sites within the Ad-AldoA 3s construct at more MOIs. Derepression started to occur at 1.1×10^5 MREs (Figure S7), a DRT about 50% lower than that observed for the Ad-AldoA 1s construct. Thus, as expected, cooperativity can be observed for miRNAs of the same family as well as for miRNAs of different families.

Among the features that we analyzed, cooperative binding of miRNAs was the only one that increased the feasibility of regulation through changes in ceRNA levels, lowering the number of competing sites needed to detect derepression by ~50%. However, this 50% difference does not seem large enough to substantially improve the prospects of observing a ceRNA effect in a physiological setting. Perhaps in unusual cases cooperativity provides more than a 50% difference, a good candidate for unusually strong cooperativity being the circular RNA CDR1as/ciRS-7 with >60 closely spaced sites to miR-7 (Hansen et al., 2013; Memczak et al., 2013). However, very few other circRNAs have more miRNA-binding sites than expected by chance (Guo et al., 2014; Rybak-Wolf et al., 2015), which brings the focus back to linear transcripts as a more abundant source of potential ceRNA candidates. For cooperativity to be a factor, such a transcript would need to be very highly expressed and have multiple sites that fall in a cooperative sequence context, and sites would need to correspond to miRNA families that are each expressed at levels sufficient to actively repress target genes. If or how frequently such conditions occur in vivo is currently unknown, but if such a candidate is found, recently developed gene-editing methods offer the opportunity to introduce precise mutations of the sites within their genomic context (without induced overexpression) and thereby provide the first convincing evidence of ceRNA regulation in vivo.

EXPERIMENTAL PROCEDURES

See Supplemental Experimental Procedures for details.

Single-Cell Reporter Assay

The fluorescent reporter plasmids are based on the pTRE-Tight-BI (Clontech) system, in which a bidirectional Tet promoter expresses eYFP and mCherry (Mukherji et al., 2011). The 3′ UTR of *mCherry* contains either zero (0s), one (1s), or

three consecutive (3s) 48-nt-long sequence stretches, which are comprised of one 8-mer MRE and ±20-bp flanking regions (Bosson et al., 2014). ESC line E14 was transfected with reporter and rtTA plasmids, induced with doxycycline 6 hr post-transfection, and harvested 18 hr later. Samples were analyzed using a FACSAria IIIu flow cytometer and eYFP and mCherry fluorescent values were corrected for autofluorescence as described in Bosson et al. (2014).

Hepatocyte Isolation and Viral Infections

Animal experiments were approved by the Kantonale Veterinäramt Zürich. Hepatocytes of 8- to 12-week-old male C57BL/6N mice (Janvier) were counted and plated at 300,000 cells per well in surface-treated six-well plates (Corning) in low-glucose media. Four to 6 hr after plating, cells were infected with adenovirus constructs in Hepatozyme media (Life Technologies) and harvested 24 hr post-infection.

Adenoviruses

Recombinant adenoviruses generated in this study are based on the *AldoA* constructs described in Denzler et al. (2014) and express *GFP* from an independent promoter. See Tables S5 and S6 for the nucleotide sequences of all Ad-AldoA constructs.

miRNA and Gene Expression Analysis

qPCRs were performed using TaqMan MicroRNA Assays (Life Technologies) for miRNA or gene-specific primer pairs (Table S4) for gene expression, respectively. Relative expression values were calculated using the ddCT method employing snoRNA202 for miRNA or mouse *36b4* (*Rplp0*) for gene expression normalization.

ACCESSION NUMBERS

The accession number for the data reported in this paper is GEO: GSE76288.

SUPPLEMENTAL INFORMATION

Supplemental Information contains Supplemental Experimental Procedures, seven figures, and six tables and can be found with this article online at http://dx.doi.org/10.1016/j.molcel.2016.09.027.

AUTHOR CONTRIBUTIONS

R.D. designed and performed experiments, analyzed and interpreted data, and drafted the manuscript. S.E.M. developed the mathematical model and performed associated analyses. A.C.T. performed RNA blots and helped with experiments shown in Figure 1. V.A. processed RNA-seq raw data. M.S. and D.P.B. designed experiments, interpreted data, and revised the manuscript. R.D., S.E.M., A.C.T., V.A., D.P.B., and M.S. reviewed the results and contributed to writing the manuscript.

ACKNOWLEDGMENTS

We would like to thank J. Zamudio, C. JnBaptise, and P. Sharp for technical advice and helpful discussions; B. Kleaveland for small-RNA-seq; and C. Ciaudo for providing ESCs. This study was supported in part by the National Science Foundation Graduate Research Fellowship (V.A.), an ERC grant "Metabolomirs" and NCCR "RNA and Biology" (M.S.), and NIH grant GM067031 (D.P.B.). D.P.B. is a Howard Hughes Medical Institute Investigator.

Received: January 25, 2016
Revised: June 10, 2016
Accepted: September 20, 2016
Published: October 27, 2016

REFERENCES

Agarwal, V., Bell, G.W., Nam, J.W., and Bartel, D.P. (2015). Predicting effective microRNA target sites in mammalian mRNAs. eLife *4*, 4.

Ala, U., Karreth, F.A., Bosia, C., Pagnani, A., Taulli, R., Léopold, V., Tay, Y., Provero, P., Zecchina, R., and Pandolfi, P.P. (2013). Integrated transcriptional and competitive endogenous RNA networks are cross-regulated in permissive molecular environments. Proc. Natl. Acad. Sci. USA *110*, 7154–7159.

Ameres, S.L., Horwich, M.D., Hung, J.H., Xu, J., Ghildiyal, M., Weng, Z., and Zamore, P.D. (2010). Target RNA-directed trimming and tailing of small silencing RNAs. Science *328*, 1534–1539.

Arvey, A., Larsson, E., Sander, C., Leslie, C.S., and Marks, D.S. (2010). Target mRNA abundance dilutes microRNA and siRNA activity. Mol. Syst. Biol. *6*, 363.

Bartel, D.P. (2009). MicroRNAs: target recognition and regulatory functions. Cell *136*, 215–233.

Bosson, A.D., Zamudio, J.R., and Sharp, P.A. (2014). Endogenous miRNA and target concentrations determine susceptibility to potential ceRNA competition. Mol. Cell *56*, 347–359.

Broderick, J.A., Salomon, W.E., Ryder, S.P., Aronin, N., and Zamore, P.D. (2011). Argonaute protein identity and pairing geometry determine cooperativity in mammalian RNA silencing. RNA *17*, 1858–1869.

Cesana, M., Cacchiarelli, D., Legnini, I., Santini, T., Sthandier, O., Chinappi, M., Tramontano, A., and Bozzoni, I. (2011). A long noncoding RNA controls muscle differentiation by functioning as a competing endogenous RNA. Cell *147*, 358–369.

Chandradoss, S.D., Schirle, N.T., Szczepaniak, M., MacRae, I.J., and Joo, C. (2015). A dynamic search process underlies microRNA targeting. Cell *162*, 96–107.

de la Mata, M., Gaidatzis, D., Vitanescu, M., Stadler, M.B., Wentzel, C., Scheiffele, P., Filipowicz, W., and Großhans, H. (2015). Potent degradation of neuronal miRNAs induced by highly complementary targets. EMBO Rep. *16*, 500–511.

Denzler, R., Agarwal, V., Stefano, J., Bartel, D.P., and Stoffel, M. (2014). Assessing the ceRNA hypothesis with quantitative measurements of miRNA and target abundance. Mol. Cell *54*, 766–776.

Doench, J.G., Petersen, C.P., and Sharp, P.A. (2003). siRNAs can function as miRNAs. Genes Dev. *17*, 438–442.

Ebert, M.S., Neilson, J.R., and Sharp, P.A. (2007). MicroRNA sponges: competitive inhibitors of small RNAs in mammalian cells. Nat. Methods *4*, 721–726.

Fabian, M.R., and Sonenberg, N. (2012). The mechanics of miRNA-mediated gene silencing: a look under the hood of miRISC. Nat. Struct. Mol. Biol. *19*, 586–593.

Franco-Zorrilla, J.M., Valli, A., Todesco, M., Mateos, I., Puga, M.I., Rubio-Somoza, I., Leyva, A., Weigel, D., García, J.A., and Paz-Ares, J. (2007). Target mimicry provides a new mechanism for regulation of microRNA activity. Nat. Genet. *39*, 1033–1037.

Garcia, D.M., Baek, D., Shin, C., Bell, G.W., Grimson, A., and Bartel, D.P. (2011). Weak seed-pairing stability and high target-site abundance decrease the proficiency of lsy-6 and other microRNAs. Nat. Struct. Mol. Biol. *18*, 1139–1146.

Giraldez, A.J., Mishima, Y., Rihel, J., Grocock, R.J., Van Dongen, S., Inoue, K., Enright, A.J., and Schier, A.F. (2006). Zebrafish MiR-430 promotes deadenylation and clearance of maternal mRNAs. Science *312*, 75–79.

Grimson, A., Farh, K.K., Johnston, W.K., Garrett-Engele, P., Lim, L.P., and Bartel, D.P. (2007). MicroRNA targeting specificity in mammals: determinants beyond seed pairing. Mol. Cell *27*, 91–105.

Guo, J.U., Agarwal, V., Guo, H., and Bartel, D.P. (2014). Expanded identification and characterization of mammalian circular RNAs. Genome Biol. *15*, 409.

Hansen, T.B., Jensen, T.I., Clausen, B.H., Bramsen, J.B., Finsen, B., Damgaard, C.K., and Kjems, J. (2013). Natural RNA circles function as efficient microRNA sponges. Nature *495*, 384–388.

Huntzinger, E., and Izaurralde, E. (2011). Gene silencing by microRNAs: contributions of translational repression and mRNA decay. Nat. Rev. Genet. *12*, 99–110.

Jens, M., and Rajewsky, N. (2015). Competition between target sites of regulators shapes post-transcriptional gene regulation. Nat. Rev. Genet. *16*, 113–126.

Karreth, F.A., Reschke, M., Ruocco, A., Ng, C., Chapuy, B., Léopold, V., Sjoberg, M., Keane, T.M., Verma, A., Ala, U., et al. (2015). The BRAF pseudogene functions as a competitive endogenous RNA and induces lymphoma in vivo. Cell *161*, 319–332.

Memczak, S., Jens, M., Elefsinioti, A., Torti, F., Krueger, J., Rybak, A., Maier, L., Mackowiak, S.D., Gregersen, L.H., Munschauer, M., et al. (2013). Circular RNAs are a large class of animal RNAs with regulatory potency. Nature *495*, 333–338.

Mukherji, S., Ebert, M.S., Zheng, G.X., Tsang, J.S., Sharp, P.A., and van Oudenaarden, A. (2011). MicroRNAs can generate thresholds in target gene expression. Nat. Genet. *43*, 854–859.

Mullokandov, G., Baccarini, A., Ruzo, A., Jayaprakash, A.D., Tung, N., Israelow, B., Evans, M.J., Sachidanandam, R., and Brown, B.D. (2012). High-throughput assessment of microRNA activity and function using microRNA sensor and decoy libraries. Nat. Methods *9*, 840–846.

Pfaff, J., Hennig, J., Herzog, F., Aebersold, R., Sattler, M., Niessing, D., and Meister, G. (2013). Structural features of Argonaute-GW182 protein interactions. Proc. Natl. Acad. Sci. USA *110*, E3770–E3779.

Poliseno, L., Salmena, L., Zhang, J., Carver, B., Haveman, W.J., and Pandolfi, P.P. (2010). A coding-independent function of gene and pseudogene mRNAs regulates tumour biology. Nature *465*, 1033–1038.

Rybak-Wolf, A., Stottmeister, C., Glažar, P., Jens, M., Pino, N., Giusti, S., Hanan, M., Behm, M., Bartok, O., Ashwal-Fluss, R., et al. (2015). Circular RNAs in the mammalian brain are highly abundant, conserved, and dynamically expressed. Mol. Cell *58*, 870–885.

Saetrom, P., Heale, B.S., Snøve, O., Jr., Aagaard, L., Alluin, J., and Rossi, J.J. (2007). Distance constraints between microRNA target sites dictate efficacy and cooperativity. Nucleic Acids Res. *35*, 2333–2342.

Salmena, L., Poliseno, L., Tay, Y., Kats, L., and Pandolfi, P.P. (2011). A ceRNA hypothesis: the Rosetta Stone of a hidden RNA language? Cell *146*, 353–358.

Salomon, W.E., Jolly, S.M., Moore, M.J., Zamore, P.D., and Serebrov, V. (2015). Single-molecule imaging reveals that Argonaute reshapes the binding properties of its nucleic acid guides. Cell *162*, 84–95.

Schirle, N.T., and MacRae, I.J. (2012). The crystal structure of human Argonaute2. Science *336*, 1037–1040.

Schmiedel, J.M., Klemm, S.L., Zheng, Y., Sahay, A., Blüthgen, N., Marks, D.S., and van Oudenaarden, A. (2015). Gene expression. MicroRNA control of protein expression noise. Science *348*, 128–132.

Xie, J., Ameres, S.L., Friedline, R., Hung, J.H., Zhang, Y., Xie, Q., Zhong, L., Su, Q., He, R., Li, M., et al. (2012). Long-term, efficient inhibition of microRNA function in mice using rAAV vectors. Nat. Methods *9*, 403–409.

Yuan, Y., Liu, B., Xie, P., Zhang, M.Q., Li, Y., Xie, Z., and Wang, X. (2015). Model-guided quantitative analysis of microRNA-mediated regulation on competing endogenous RNAs using a synthetic gene circuit. Proc. Natl. Acad. Sci. USA *112*, 3158–3163.

Molecular Cell, Volume *64*

Supplemental Information

Impact of MicroRNA Levels, Target-Site Complementarity, and Cooperativity on Competing Endogenous RNA-Regulated Gene Expression

Rémy Denzler, Sean E. McGeary, Alexandra C. Title, Vikram Agarwal, David P. Bartel, and Markus Stoffel

Figure S1
Denzler et al.

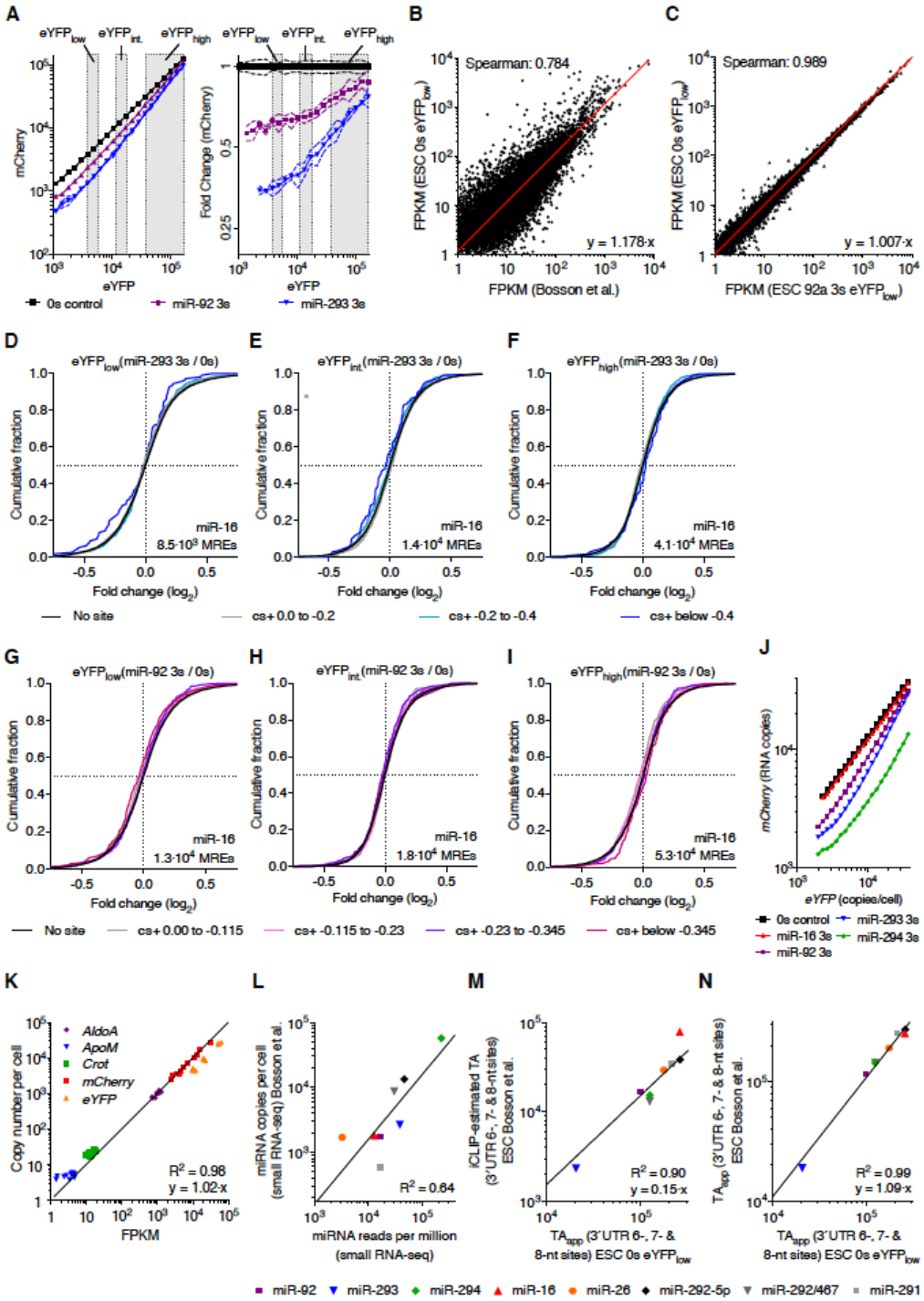

Figure S1. Embryonic Stem Cells (ESCs) Characterized in Bosson et al. (2014) Are Very Similar to ESCs Used in this Study. Related to Figure 1.

(A) ESCs transfected (n = 2) with a 3s reporter for miR-293 (blue) or miR-92 (purple), or a 0s reporter control. Mean mCherry fluorescence (left), and mCherry fluorescence normalized to 0s control (right) across 20 bins of eYFP. In the right panel only fold-change values with mean mCherry expression above 0.8×10^3 are shown. Cells were analyzed and sorted into three bins based on their eYFP expression. The respective gates for $eYFP_{low}$, $eYFP_{int.}$, and $eYFP_{high}$ are highlighted in grey.

(B) Relationship between fragments per kilobase of transcript per million fragments mapped (FPKM) from ESCs of published RNA sequencing (RNA-seq) data (Bosson et al., 2014) and ESCs transfected with the 0s reporter and sorted for low eYFP expressing cells. Line represents linear regression of data points; respective equation is shown.

(C) Relationship between FPKM from RNA-seq data of 0s- and miR-92 3s-transfected ESCs, sorted for low eYFP expressing cells. Line represents linear regression of data points; respective equation is shown.

(D–I) RNA-seq results of sorted ESCs shown in (A) and Figures 1D–1I. ESCs were transfected with a 3s reporter for miR-293 (D–F), or miR-92 (G–I), and gated for cells with low eYFP (D, G), intermediate eYFP (E, H), or high eYFP (F, I) expression. Cumulative distribution function (CDF) of mRNA changes for predicted target genes of miR-16 (D–I) with the indicated context+ score (cs+) bins (color) or for genes with no respective miRNA site (black). miRNA response elements (MREs) per cell evaluated by absolute quantification of *mCherry* by qPCR are shown on each graph. *p < 0.05, **p < 0.01, ***p < 0.001, ****p < 0.0001, one-sided Kolmogorov–Smirnov (K–S) test.

(J) ESCs transfected with the 0s control or 3s reporter constructs (n = 3) with miRNA-binding sites for miR-16, miR-294, miR-293, or miR-92. Protein fluorescence values shown in Figure 1B have been transformed to RNA copies per cell using the equations shown in Figure 1J.

(K) Relationship between FPKM from RNA-seq data and absolute quantification using qPCR. Represented are five genes quantified in 12 ESC samples. Line represents linear regression of data points; respective equation is shown.

(L) Relationship between small RNA-seq data from published ESCs (Bosson et al., 2014) and of ESCs used in this study. See also Table S2.

(M) Relationship between apparent target abundance (TA_{app}) of ESCs transfected with the 0s reporter and sorted for low eYFP expressing cells (ESC 0s $eYFP_{low}$) and iCLIP-estimated TA from published ESCs (Bosson et al., 2014). Line represents linear regression of data points; respective equation is shown.
(N) Relationship between TA_{app} from ESCs of published RNA-seq data (Bosson et al., 2014) and ESC 0s $eYFP_{low}$. FPKM from Bosson et al. (2014) have been transformed using equation shown in Figure (B). Line represents linear regression of data points; respective equation is shown.
Data represent mean ± SEM for Figures (A) and (J).

Figure S2
Denzler et al.

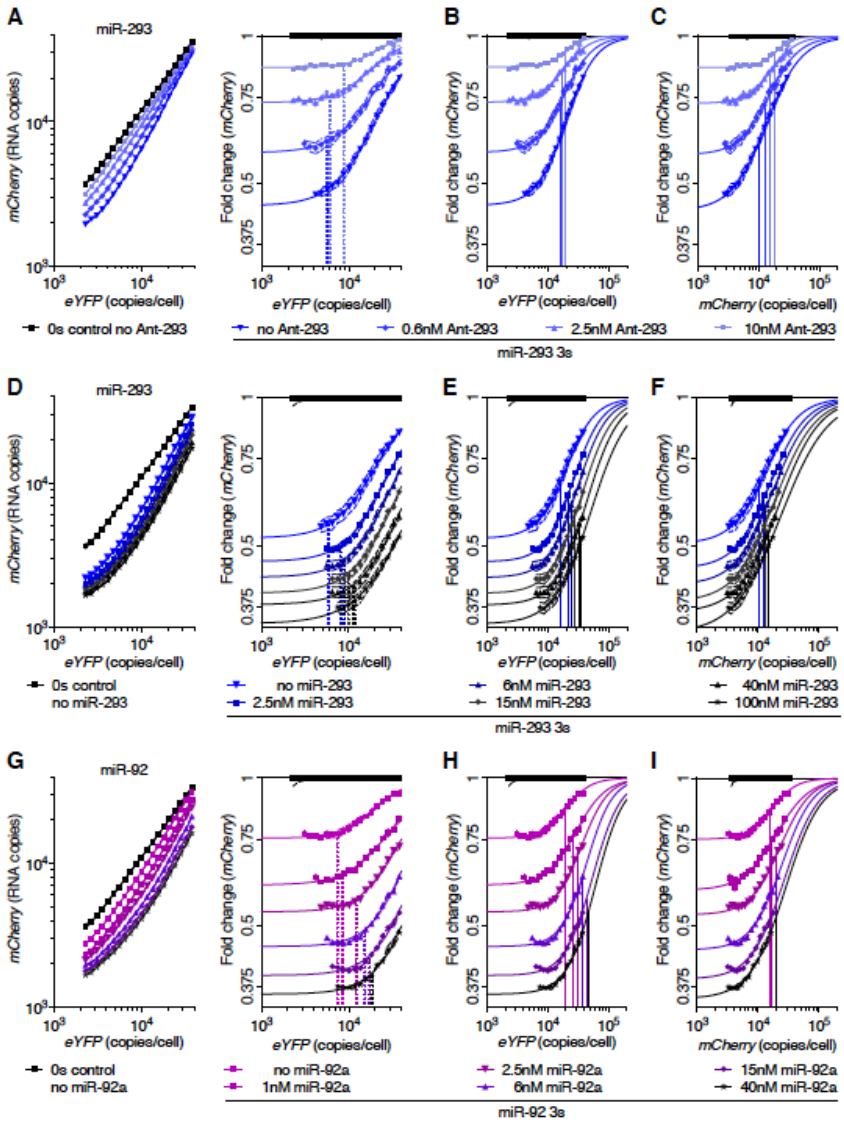

Figure S2. Derepression Threshold Values are Insensitive to Changes in miRNA Activity. Related to Figure 2.

(A–I) ESCs co-transfected with 3s-reporter for miR-293 (A–F), miR-92 (G–I) or respective 0s reporter control, and different concentrations of Antagomir-293 (Ant-293) (n = 3) (A–C), miR-293 (n = 6) (D–F), or miR-92 (n = 6) (G–I). Protein fluorescence values shown in Figures 2A, 2C, and 2E have been transformed to RNA copies per cell using the equations in Figure 1J.

(A, D, G) Mean transformed *mCherry* (left), and *mCherry* normalized to 0s control (right) across 20 bins of *eYFP*. All 3s reporter co-transfections have been normalized to the 0s control with the same respective Ant-293 or miRNA concentration. One representative 0s control where no Ant-293 or miRNA has been transfected is shown. Vertical, dotted lines denote *eYFP* values at the derepression threshold (DRT).

(B, E, H) Data shown in (A, D, G), with vertical lines denoting *eYFP* values where half-maximal derepression (termed half maximal inhibitory concentration, or IC_{50}) is observed. At first glance, a uniform IC_{50} in the context of declining miR-293 activity supports the mixed-affinity model, in which the effective target concentration does not change as miRNA concentrations decreases. However, we cannot exclude the possibility that this interpretation is confounded by the use of co-transfection in this experiment, in which cells that received more plasmid, and thus had more eYFP expression, might have also taken up more Ant-293, and thus would have experienced more miR-293 repression.

(C, F, I) Data shown in Figures 2B, 2D, and 2F, with vertical lines denoting *mCherry* values where half-maximal derepression is observed. Although the IC_{50} values increased only slightly as more miRNA was transfected, interpretation was again potentially confounded by co-transfection of plasmid and miRNA, in which cells that received more plasmid might have also received more miRNA.

Data represent mean ± SEM for all panels.

Figure S3
Denzler et al.

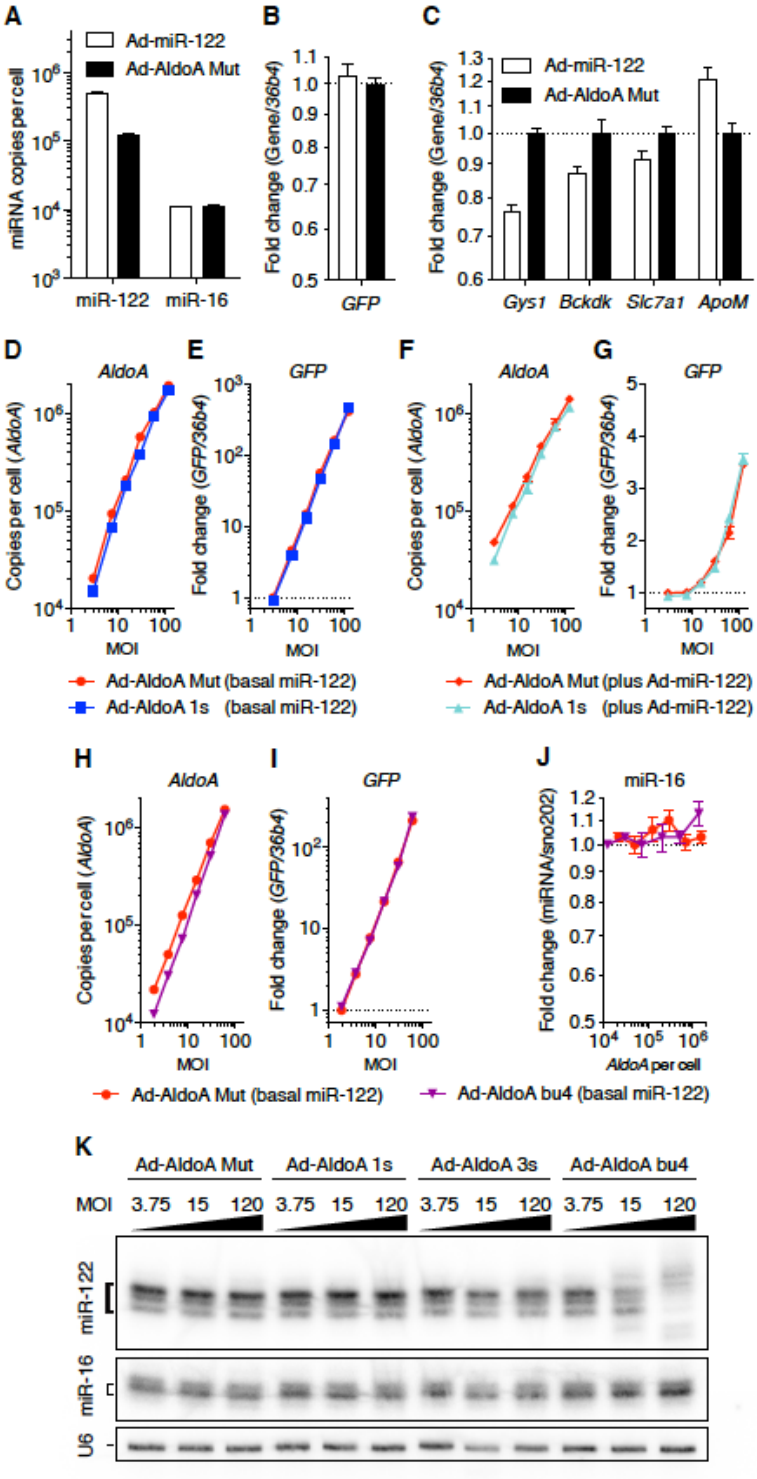

Figure S3. Increasing miR-122 Levels Increases miR-122 Target Gene Repression. Related to Figure 3.

(A–C) Primary hepatocytes (n = 4) infected at a multiplicity of infection (MOI) of 50 with an adenovirus expressing miR-122 (Ad-miR-122) or with Ad-AldoA Mut. Absolute miRNA copy numbers per cell (A), relative *GFP* expression (B), or relative expression of miR-122 target genes and control non-target genes (*ApoM*) (C) normalized to Ad-AldoA Mut.

(D–G) Primary hepatocytes (n = 4) infected with different MOIs of Ad-AldoA Mut or 1s at basal miR-122 levels (D, E), or in addition to MOI 50 of Ad-miR-122 (F, G). Absolute copy numbers per cell of *AldoA* (D, F), and relative gene expression of *GFP* (E, G).

(H–J) Primary hepatocytes (n = 4) infected with different MOIs of Ad-AldoA Mut or bu4 at basal miR-122 levels. Absolute copy numbers per cell of *AldoA* (H), relative gene expression of *GFP* (I), and relative expression of miR-16 (J). miRNA expression is relative to the lowest MOI of Ad-AldoA Mut.

(K) Northern blot analysis of miR-122, miR-16 and U6 of hepatocytes infected with MOI 3.75, MOI 15, and MOI 120 of Ad-AldoA Mut, bu4, 1s, or 3s.

GFP expression is relative to Ad-AldoA Mut at the lowest MOI. Data represent mean ± SEM for all panels.

Figure S4
Denzler et al.

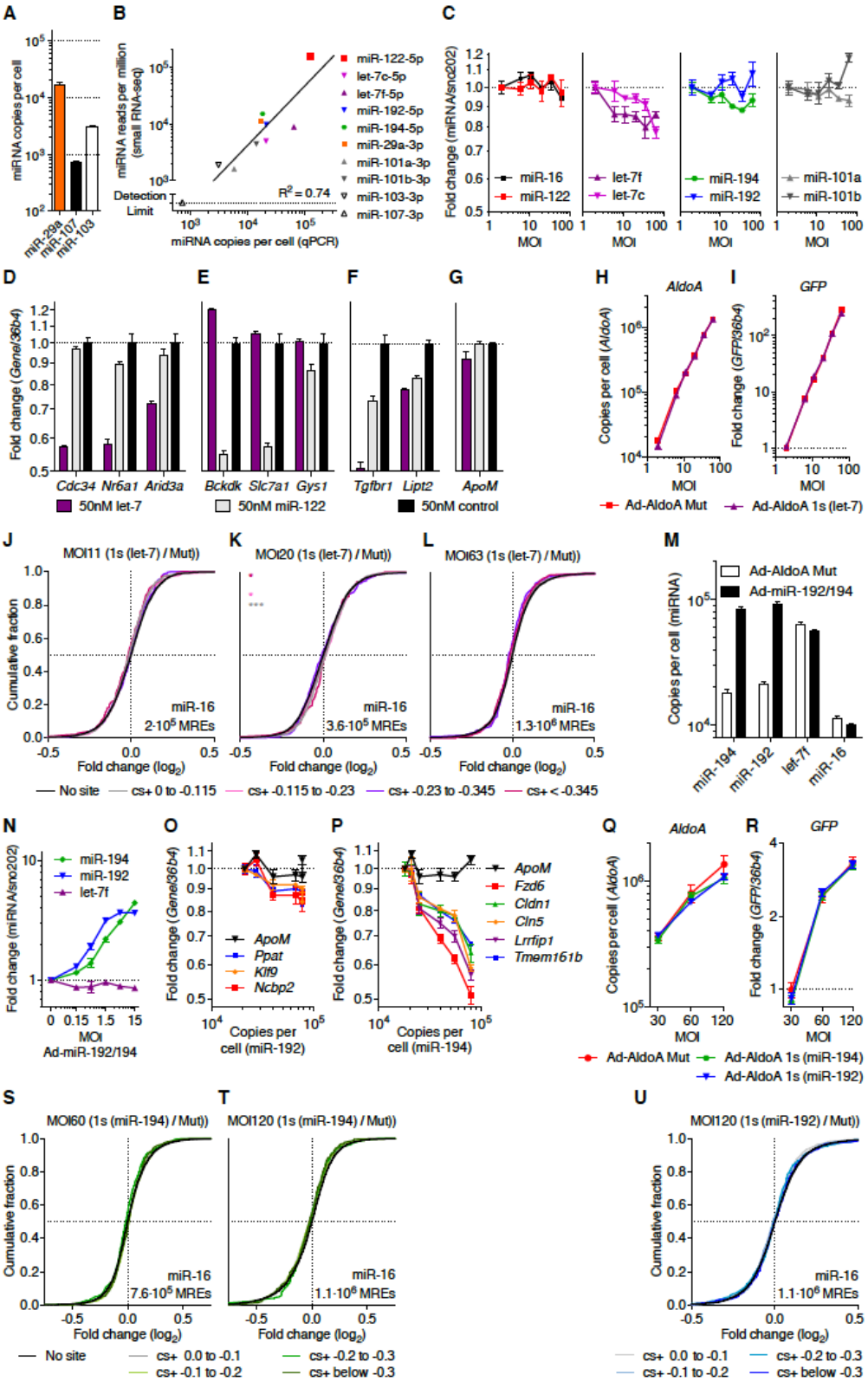

Figure S4. Experimental Evaluation of Predicted Target Genes of miR-122, let-7 miR-192 and miR-194 in Primary Hepatocytes. Related to Figure 4.

(A) Absolute copies per cell of hepatocyte miRNAs (n = 3).

(B) Relationship between miRNA counts from small RNA-seq data and absolute miRNA copies of primary hepatocytes. Line represents linear regression of data points. See also Table S2.

(C) Relative miRNA expression of hepatocytes (n = 4) infected with different MOIs of Ad-AldoA Mut. miRNA expression is relative to Ad-AldoA Mut at MOI 2.

(D–G) Primary hepatocytes transfected with 50 nM of let-7, miR-122, or control siRNA. Relative gene expression of predicted target genes of let-7 (D), of miR-122 (E), or of miR-122 and let-7 (F), and a control non-target gene (*ApoM*) (G). Gene expression is normalized to the negative control.

(H–L) Primary hepatocytes infected with different MOIs of Ad-AldoA Mut or 1s (let-7). Absolute copy numbers per cell of *AldoA* (H), or relative gene expression of *GFP* (I). RNA-seq results (n = 2) from hepatocytes infected with MOI 11 (J), MOI 20 (K), or MOI 63 (L) of Ad-AldoA Mut or 1s (let-7) shown in Figures 4C–4F. CDF of mRNA changes for predicted target genes of miR-16 with the indicated cs+ bins (color) or for genes with no respective miRNA site (black).

(M–P) Primary hepatocytes infected with different MOIs of an adenovirus (n = 4) expressing the bicistronic miR-192/-194 (Ad-miR-192/194) (Krutzfeldt et al., 2012). To control for virus dependent effects, Ad-miR-192/194 was complemented with Ad-AldoA Mut to retrieve a constant MOI of 100. (M) Absolute miRNA copy numbers per cell at MOI 15 of Ad-miR-192/194. Relative miRNA levels (N), relative expression of predicted target genes of miR-192 (O), or of miR-194 (P) and a control non-target gene (*ApoM*) normalized to MOI 100 of Ad-AldoA Mut.

(Q–U) Primary hepatocytes (n = 4) infected with different MOIs of Ad-AldoA Mut, 1s (miR-192), or 1s (miR-194) in addition to MOI 15 Ad-miR-192/194. Absolute copy numbers per cell of *AldoA* (Q), and relative gene expression of *GFP* (R). RNA-seq results (n = 2) from hepatocytes infected with MOI 60 (S) or MOI 120 (T) of Ad-AldoA 1s (miR-194), MOI 120 of Ad-AldoA 1s (miR-192) (U), or respective Ad-AldoA Mut controls. CDF of mRNA changes for predicted target genes of miR-16 with the indicated cs+ bins (color) or for genes with no respective miRNA site (black). *GFP* expression is relative to Ad-AldoA Mut at the lowest MOI. Data represent mean ± SEM for Figures (A), (C–I), and (M–R). MREs per cell evaluated by absolute quantification of *AldoA* by qPCR are shown on each CDF graph. *p < 0.05, **p < 0.01, ***p < 0.001, ****p < 0.0001, one-sided K–S test.

Figure S5
Denzler et al.

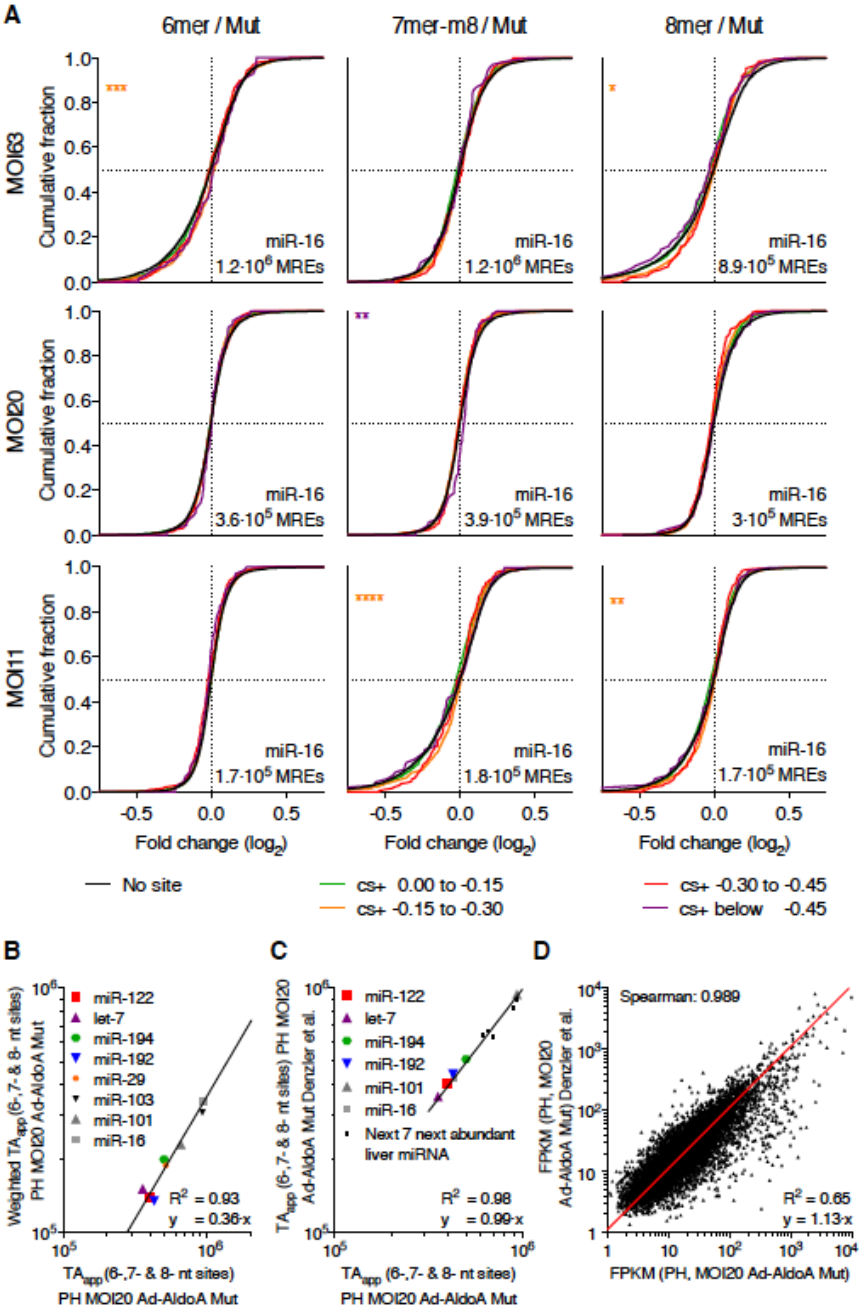

Figure S5. TA_{app} of Primary Hepatocytes Described in Denzler et al. (2014) Is Comparable to that of this Study. Related to Figure 5.

(A) RNA-seq results (n = 2) showing derepression of predicted targets from hepatocytes infected with MOI 11, MOI 20, or MOI 63 of Ad-AldoA miR-122 8mer, miR-122 7mer-m8, miR-122 6mer, or Mut shown in Figure 5E. CDF of mRNA changes for predicted target genes of miR-16 with the indicated cs+ bins (color) or for genes with no respective miRNA site (black). MREs per cell evaluated by absolute quantification of *AldoA* by qPCR are shown on each graph. *p < 0.05, **p < 0.01, ***p < 0.001, ****p < 0.0001, one-sided K–S test.

(B) Relationship between weighted TA_{app} and TA_{app} of primary hepatocytes (PH) infected with MOI 20 of Ad-AldoA Mut. Line represents linear regression of data points.

(C and D) Relationship between RNA-seq data from this study and of published work (Denzler et al., 2014). Comparison of transcriptome TA_{app} (A) and FPKM (B) of primary hepatocytes (PH) infected with MOI 20 of Ad-AldoA Mut. Line represents linear regression of data points.

Figure S6
Denzler et al.

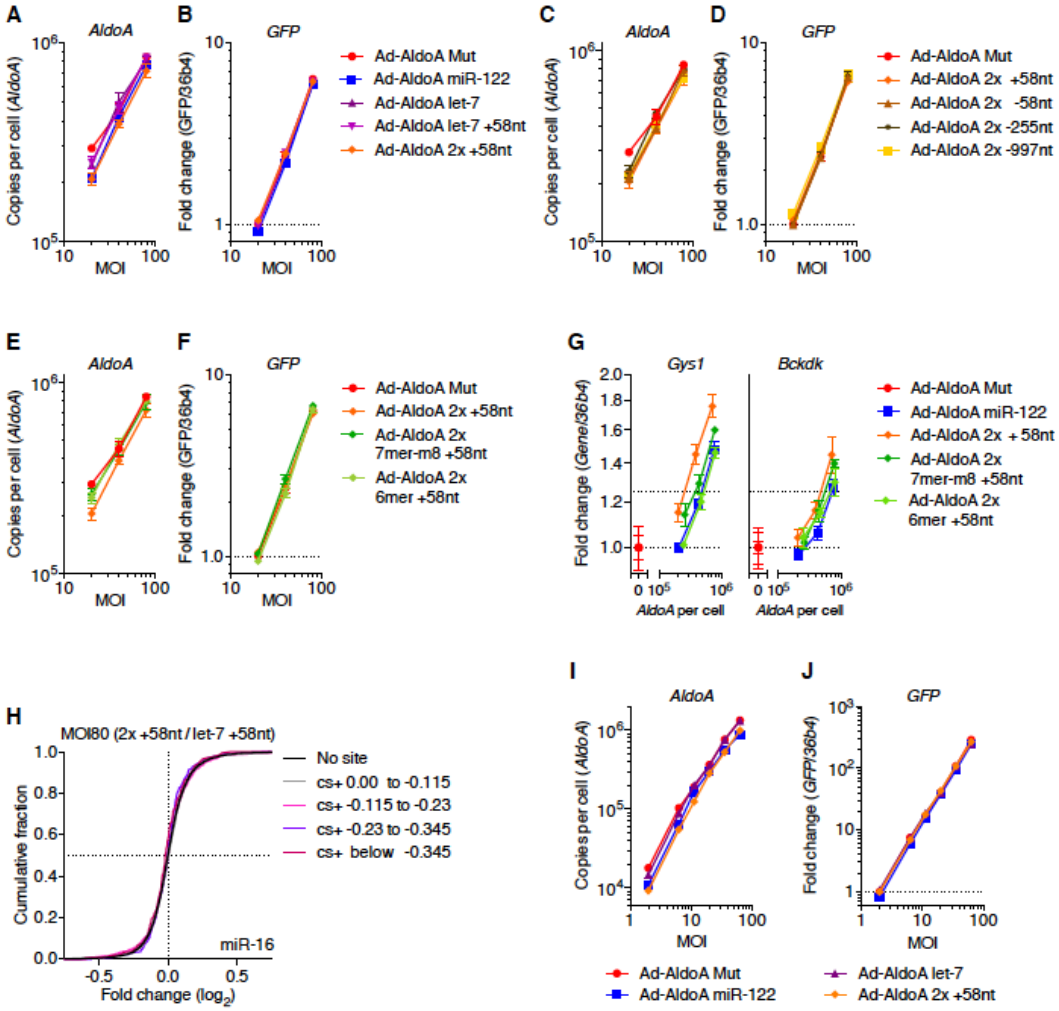

Figure S6. Overview of Ad-AldoA Constructs Harboring Seed Matches for Two Different miRNA Families. Related to Figure 6.

(A–J) Primary hepatocytes infected with different MOIs of Ad-AldoA Mut, miR-122, let-7, let-7 +58nt, 2x +58nt, 2x -58nt, 2x -255nt, 2x -997nt, 2x 7mer-m8 +58nt, or 2x 6mer +58nt. Absolute copy numbers per cell of *AldoA* (A, C, E, I), relative gene expression of *GFP* (B, D, F, J), and relative gene expression of miR-122 target genes (G). *GFP* are relative to Ad-AldoA Mut at the lowest MOI. Data represent mean ± SEM (n = 4). (H) RNA-seq results (n = 2) showing derepression of predicted targets from hepatocytes infected with MOI 80 of Ad-AldoA let-7 +58nt or 2x +58nt shown in Figure 6J. CDF of mRNA changes for predicted target genes of miR-16 with the indicated cs+ bins (color) or for genes with no respective miRNA site (black). MREs per cell evaluated by absolute quantification of *AldoA* by qPCR are shown on each graph. *p < 0.05, **p < 0.01, ***p < 0.001, ****p < 0.0001, one-sided K–S test.

Figure S7
Denzler et al.

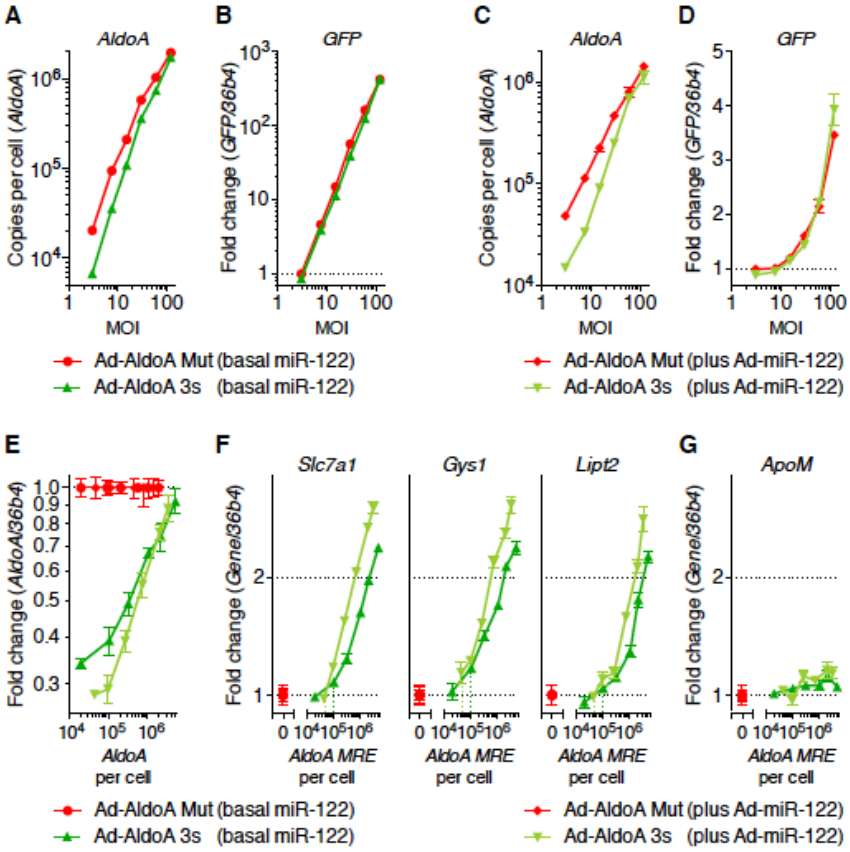

Figure S7. Derepression Is Enhanced when Mediated by Closely Spaced MREs of the Same miRNA Family. Related to Figure 3.

(A–G) Primary hepatocytes infected with different MOIs of Ad-AldoA Mut or 3s (n = 4) at basal miR-122 levels (A, B, and E–G), or in addition to MOI 50 of Ad-miR-122 (C–G). Absolute copy numbers per cell of *AldoA* (A, C), relative gene expression of *GFP* (B, D), *AldoA* (E), miR-122 target genes (F) or a control non-target gene (*ApoM*) (G). Data represent mean ± SEM (n = 4) for all panels.

Table S1: Gene Expression Levels, Fold Changes, and Predicted Target Site Efficacy Scores (context+ scores) across all Embryonic Stem Cell RNA-seq Samples. Related to Figures 1 and S1.

Table S2: miRNA Counts and RPM of Embryonic Stem Cells and Primary Hepatocyte Small RNA-seq Samples. Related to Figures 1, 4, S1 and S4.

Table S3: Gene Expression Levels, Fold Changes, and Predicted Target Site Efficacy Scores (context+ scores) across all Primary Hepatocyte RNA-seq Samples. Related to Figures 4, 5, 6, S4, S5, and S6.

Table S4: Primer Sets, siRNA and Northern Blot Probes Used in this Study. Related to Figures 1, 3, 4, 5, 6, S1, S3, S4, S5, S6, and S7.

Name	Sequence (5' to 3')
36b4 f	GCCGTGATGCCCAGGGAAGACA
36b4 r	CATCTGCTTGGAGCCCACGTTG
ApoM f	CCCAGACATGAAAACAGACCT
ApoM r	GGGTGTGGTGACCGATTG
AldoA f	GCGCTGTGTGCTAAAGATTG
AldoA r	AGGCTCCACAATGGGTACAA
Crot f	AGTGAAGGGCATTGTCCAAC
Crot r	TCTTGTGGATATATGTCAATTGTCTG
mCherry f	GCGTGATGAACTTCGAGGA
mCherry r	GATGAACTCGCCGTCCTG
eYFP f	GGACTGGTAGCTCAGGTAGTGG
eYFP r	CAGCAGAACACCCCCATC
GFP f	CACTACCTGAGCACCCAGTC
GFP r	TTGTACAGCTCGTCCATGCC
Gys1 f	GGTGTGAGGACGCAGGTAG
Gys1 r	GCCAACGCCCAAAATACA
Slc7a1 f	ATTTCAGCCGGCCTCCTA
Slc7a1 r	TGCCCACAGTGTCCCTTC
P4ha1 f	CGTGGGGAGGGTATCAAAAT
P4ha1 r	ATGGTAGCGGCAGAACAGTC
Ndrg3 f	TCCTGGCCAACAAGAAGC
Ndrg3 r	CTCATCCATGGTGGGGTACT
Tmed3 f	GGTCACGGCTCTCACTCAG
Tmed3 r	TCACAGTCTTCAGAGCCTCGT
Bckdk f	GAGAAGTGGGTGGATTTTGC
Bckdk r	ATGGGAATGAAGGGGAACC
Lipt2 f	CCCTACACTGGCGTCTGG
Lipt2 r	CATGTGAGGTCGGTTGAACA
Tgfbr1 f	GCAGCTCCTCATCGTGTTG
Tgfbr1 r	AGAGGTGGCAGAAACACTGTAAT
Nr6a1 f	GCTTGCCAGAGATCCGATAC
Nr6a1 r	AGTGCAGCACCACCTTAAAGA
Cdc34 f	GGAAGGACCGCGAGTACA
Cdc34 r	AGTACTCGGCCAGCGTAGTG
Arid3a f	ACCATGGGGACTGGACCT
Arid3a r	GGTCCGCATCCAGTTCATA
Fzd6 f	TTAAGCGAAACCGCAAGC
Fzd6 r	TTGGAAATGACCTTCAGCCTA
Cln5 f	ACTACAAGCCCCGATTTGG
Cln5 r	ACGGCGTCATGCATAAGTTT
Lrrfip1 f	GGCCAAATGTGAGCAACAG
Lrrfip1 r	CCTTGTGTGACTCGATCTGC
Cldn1 f	ACTCCTTGCTGAATCTGAACAGT
Cldn1 r	GGACACAAAGATTGCGATCAG

Tmem161b f	CCACCGTTGGGTAGAGAGAG
Tmem161b r	GCAGGTGACTTCGCATCAT
Ppat f	CTAGATGTGCCGCATGTGAT
Ppat r	AATACCAGCGCTCTCCTGAC
Klf9 f	CTCCGAAAAGAGGCACAAGT
Klf9 r	GCGAGAACTTTTTAAGGCAGTC
Ncbp2 f	TAAGGAGGGCAGGCAGTATG
Ncbp2 r	TTTTGTGCCAGTTTCCCATAG
Northern probe miR-122	CAAACACCATTGTCACACTCCA
Northern probe miR-16	CGCCAATATTTACGTGCTGCTA
Northern probe U6	CTCTGTATCGTTCCAATTTTAGTATA
miR-293 mimic	AGUGCCGCAGAGUUUGUAGUGU
miR-92a mimic	UAUUGCACUUGUCCCGGCCUG
miR-122 mimic	UGGAGUGUGACAAUGGUGUUUG
let-7f mimic	UGAGGUAGUAGAUUGUAUAGUU
Negative control siRNA 1	UGGUUUACAUGUCGACUAA
Negative control siRNA 2	UGGUUUACAUGUUGUGUGA
Negative control siRNA 3	UGGUUUACAUGUUUUCUGA
Negative control siRNA 4	UGGUUUACAUGUUUUCCUA

Table S5: 3′ UTR Sequences of Adenovirus Constructs that Harbor miRNA-Binding Sites After the Endogenous Stop Codon of AldoA.

Related to Figures 4, 5, 6, S4, S5, S6, and S7

All relevant miRNA-binding sites are highlighted in bold and colored by miRNA family: miR-122 (blue), let-7 (purple), miR-101 (grey), miR-194 (green), miR-192 (light blue), and mutated control (red). Emphasized in bold are the start codon, and the naturally occurring (TAA) or artificially introduced (TGA) stop codon. Underlined text shows translated polypeptide. The three stars indicate where the endogenous 3′ UTR of AldolaseA variant 2 starts.

Construct name	Sequence (5' to 3')
Shared sequence for all Ad-AldoA viruses shown in this table	CAGCTGAATAGGCTGCGTTCTCTTGGAACGCGCAGCAGAACGAGGTTCTGGTGACCCTAGCCGCGTTC GCTCCTTAGTCCTTTCGCCTACCCACCGGCGTACCAGGCAGACCCACCCCGTCCTGTGCCAGGAAAGC ACTGCCACCGGCACC**ATG**CCCCACCCATACCCAGCACTGACC**TGA**GAGCAGAAGAAGGAGCTGTCTGA CATCGCTCACCGCATTGTGGCTCCGGGCAAGGGCATCCTGGCTGCAGATGAGTCCACCGGAAGCATTG CCAAGCGCCTGCAGTCCATTGGCACCGAGAACACCGAGGAGAACAGGCGCTTCTACCGCCAGCTGCTG CTGACTGCAGACGACCGTGTGAATCCCTGCATTGGGGGGGTGATCCTCTTCCACGAGACACTGTACCA GAAGGCAGATGATGGACGTCCCTTCCCCCAAGTTATCAAGTCCAAGGGTGGTGTTGTGGGCATTAAGG TAGATAAGGGTGTGGTGCCCCTGGCAGGAACCAATGGCGAGACAACTACCCAGGGGCTGGATGGGCTG TCTGAACGCTGTGCCCAGTATAAGAAGGATGGAGCCGACTTTGCCAAGTGGCGCTGTGTGCTAAAGAT TGGGGAACATACTCCCTCGGCCCTGGCCATCATGGAAAATGCCAATGTTCTGGCCCGTTATGCCAGCA TCTGCCAGCAGAATGGCATTGTACCCATTGTGGAGCCTGAAATTCTCCCTGATGGGGACCATGACTTG AAGCGCTGCCAGTATGTTACTGAGAAGGTCCTGGCGGCTGTCTACAAGGCTCTGAGCGACCACCATGT CTATCTGGAAGGCACATTGCTGAAGCCCAACATGGTCACCCCTGGCCATGCTTGCACCCAGAAATTTT CCAATGAGGAGATTGCCATGGCAACGGTCACAGCACTTCGTCGCACAGTGCCCCCTGCTGTCACTGGG GTCACTTTCCTGTCTGGAGGGCAGAGTGAGGAAGAGGCATCCATCAACCTCAATGCTATCAACAAGTG CCCCCTGCTGAAGCCATGGGCCTTGACTTTCTCCTATGGTCGAGCCCTGCAGGCCTCTGCTCTAAAGG CCTGGGGTGGGAAGAAGGAGAACCTGAAGGCAGCCCAGGAGGAGTACATCAAGCGCGCCCTGGCCAAC AGCCTCGCTTGTCAAGGAAAGTATACCCCAAGTGGCCAGTCTGGAGCCGCAGCCAGTGAATCTCTCTT CATCTCTAACCATGCCTAC**TAA*****

Ad-AldoA Mut	**TAA*****CCAGAGCTGAACTAAGGCTGCTCCATCA**ACCATAAA**CGCGTCTGCCTACCCACTTGCTATTG AAGAGGGGTCTTCAGGCTCTTTCCCATCACTCTTGCTGCTGCCCTCGTGTGCGGTGTTGTCTGTGAAT GCTAAATCTGCCATCCCTTCCAGCCCACTGCCAATAAACAACTATTTAAGGGGGAAAAAAA
Ad-AldoA miR-122 (8mer)	**TAA*****CCAGAGCTGAACTAAGGCTGCTCCATCA**ACACTCCA**CGCGTCTGCCTACCCACTTGCTATTG AAGAGGGGTCTTCAGGCTCTTTCCCATCACTCTTGCTGCTGCCCTCGTGTGCGGTGTTGTCTGTGAAT GCTAAATCTGCCATCCCTTCCAGCCCACTGCCAATAAACAACTATTTAAGGGGGAAAAAAA
Ad-AldoA miR-122 (7mer-m8)	**TAA*****CCAGAGCTGAACTAAGGCTGCTCCATCA**ACACTCC**TCGCGTCTGCCTACCCACTTGCTATTG AAGAGGGGTCTTCAGGCTCTTTCCCATCACTCTTGCTGCTGCCCTCGTGTGCGGTGTTGTCTGTGAAT GCTAAATCTGCCATCCCTTCCAGCCCACTGCCAATAAACAACTATTTAAGGGGGAAAAAAA
Ad-AldoA miR-122 (6mer)	**TAA*****CCAGAGCTGAACTAAGGCTGCTCCATCAT**CACTCC**TCGCGTCTGCCTACCCACTTGCTATTG AAGAGGGGTCTTCAGGCTCTTTCCCATCACTCTTGCTGCTGCCCTCGTGTGCGGTGTTGTCTGTGAAT GCTAAATCTGCCATCCCTTCCAGCCCACTGCCAATAAACAACTATTTAAGGGGGAAAAAAA
Ad-AldoA 3s (miR-122)	**TAA*****CCAGAGCTGAACTAAGGCTGCTCCATCA**ACACTCCA**CGCGAGCTGCTCCATCA**ACACTCCA**C GCGAGCTGCTCCATCA**ACACTCCA**CGCGTCTGCCTACCCACTTGCTATTGAAGAGGGGTCTTCAGGCT CTTTCCCATCACTCTTGCTGCTGCCCTCGTGTGCGGTGTTGTCTGTGAATGCTAAATCTGCCATCCCT TCCAGCCCACTGCCAATAAACAACTATTTAAGGGGGAAAAAAA
Ad-AldoA bu4 (miR-122)	**TAA*****CCAGAGCTGAACTA**CAAACACCAT**ATCA**ACACTCCA**CGCGTCTGCCTACCCACTTGCTATTG AAGAGGGGTCTTCAGGCTCTTTCCCATCACTCTTGCTGCTGCCCTCGTGTGCGGTGTTGTCTGTGAAT GCTAAATCTGCCATCCCTTCCAGCCCACTGCCAATAAACAACTATTTAAGGGGGAAAAAAA
Ad-AldoA let-7	**TAA*****CCAGAGCTGAACTAAGGCTGCTCCATCA**CTACCTCA**CGCGTCTGCCTACCCACTTGCTATTG AAGAGGGGTCTTCAGGCTCTTTCCCATCACTCTTGCTGCTGCCCTCGTGTGCGGTGTTGTCTGTGAAT GCTAAATCTGCCATCCCTTCCAGCCCACTGCCAATAAACAACTATTTAAGGGGGAAAAAAA
Ad-AldoA let-7 +58nt	**TAA*****CCAGAGCTGAACTAAGGCTGCTCCATCA**ACCATAAA**CGCGTCTGCCTACCCACTTGCTATTG AAGAGGGGTCTTCAGGCTCTTTCCCATCACTC**CTACCTCA**GCCCTCGTGTGCGGTGTTGTCTGTGAAT GCTAAATCTGCCATCCCTTCCAGCCCACTGCCAATAAACAACTATTTAAGGGGGAAAAAAA
Ad-AldoA miR-101	**TAA*****CCAGAGCTGAACTAAGGCTGCTCCATCA**GTACTGTA**CGCGTCTGCCTACCCACTTGCTATTG AAGAGGGGTCTTCAGGCTCTTTCCCATCACTCTTGCTGCTGCCCTCGTGTGCGGTGTTGTCTGTGAAT GCTAAATCTGCCATCCCTTCCAGCCCACTGCCAATAAACAACTATTTAAGGGGGAAAAAAA
Ad-AldoA miR-194	**TAA*****CCAGAGCTGAACTAAGGCTGCTCCATCA**CTGTTACA**CGCGTCTGCCTACCCACTTGCTATTG AAGAGGGGTCTTCAGGCTCTTTCCCATCACTCTTGCTGCTGCCCTCGTGTGCGGTGTTGTCTGTGAAT GCTAAATCTGCCATCCCTTCCAGCCCACTGCCAATAAACAACTATTTAAGGGGGAAAAAAA
Ad-AldoA miR-192	**TAA*****CCAGAGCTGAACTAAGGCTGCTCCATCA**TAGGTCAA**CGCGTCTGCCTACCCACTTGCTATTG AAGAGGGGTCTTCAGGCTCTTTCCCATCACTCTTGCTGCTGCCCTCGTGTGCGGTGTTGTCTGTGAAT GCTAAATCTGCCATCCCTTCCAGCCCACTGCCAATAAACAACTATTTAAGGGGGAAAAAAA
Ad-AldoA 2x +58nt	**TAA*****CCAGAGCTGAACTAAGGCTGCTCCATCA**ACACTCCA**CGCGTCTGCCTACCCACTTGCTATTG AAGAGGGGTCTTCAGGCTCTTTCCCATCACTC**CTACCTCA**GCCCTCGTGTGCGGTGTTGTCTGTGAAT GCTAAATCTGCCATCCCTTCCAGCCCACTGCCAATAAACAACTATTTAAGGGGGAAAAAAA
Ad-AldoA 2x 7mer-m8 +58nt	**TAA*****CCAGAGCTGAACTAAGGCTGCTCCATCA**ACACTCC**TCGCGTCTGCCTACCCACTTGCTATTG AAGAGGGGTCTTCAGGCTCTTTCCCATCACTC**CTACCTCA**GCCCTCGTGTGCGGTGTTGTCTGTGAAT GCTAAATCTGCCATCCCTTCCAGCCCACTGCCAATAAACAACTATTTAAGGGGGAAAAAAA
Ad-AldoA 2x 6mer +58nt	**TAA*****CCAGAGCTGAACTAAGGCTGCTCCATCAT**CACTCC**TCGCGTCTGCCTACCCACTTGCTATTG AAGAGGGGTCTTCAGGCTCTTTCCCATCACTC**CTACCTCA**GCCCTCGTGTGCGGTGTTGTCTGTGAAT GCTAAATCTGCCATCCCTTCCAGCCCACTGCCAATAAACAACTATTTAAGGGGGAAAAAAA

Table S6: 3′ UTR Sequences of Adenovirus Constructs that Harbor a miRNA-Site Before the Endogenous Stop Codon of AldoA. Related to Figures 6 and S6.

In bold and colors are miR-122 (blue) and let-7 (purple) binding sites, emphasized in bold are the start codon, and the naturally occurring (TAA) or artificially introduced (TGA) stop codon. Underlined text shows translated polypeptide. The three stars indicate where the endogenous 3′ UTR of AldolaseA variant 2 starts.

Construct name	Sequence (5' to 3')
Ad-AldoA 2x -58nt	CAGCTGAATAGGCTGCGTTCTCTTGGAACGCGCAGCAGAACGAGGTTCTGGTGACCCTAGCCGCGTTCG CTCCTTAGTCCTTTCGCCTACCCACCGGCGTACCAGGCAGACCCACCCCGTCCTGTGCCAGGAAAGCAC TGCCACCGGCACC**ATG**CCCCACCCATACCCAGCACTGACC**TGA**GAGCAGAAGAAGGAGCTGTCTGACAT CGCTCACCGCATTGTGGCTCCGGGCAAGGGCATCCTGGCTGCAGATGAGTCCACCGGAAGCATTGCCAA GCGCCTGCAGTCCATTGGCACCGAGAACACCGAGGAGAACAGGCGCTTCTACCGCCAGCTGCTGCTGAC TGCAGACGACCGTGTGAATCCCTGCATTGGGGGGGTGATCCTCTTCCACGAGACACTGTACCAGAAGGC AGATGATGGACGTCCCTTCCCCCAAGTTATCAAGTCCAAGGGTGGTGTTGTGGGCATTAAGGTAGATAA GGGTGTGGTGCCCCTGGCAGGAACCAATGGCGAGACAACTACCCAGGGGCTGGATGGGCTGTCTGAACG CTGTGCCCAGTATAAGAAGGATGGAGCCGACTTTGCCAAGTGGCGCTGTGTGCTAAAGATTGGGGAACA TACTCCCTCGGCCCTGGCCATCATGGAAAATGCCAATGTTCTGGCCCGTTATGCCAGCATCTGCCAGCA GAATGGCATTGTACCCATTGTGGAGCCTGAAATTCTCCCTGATGGGGACCATGACTTGAAGCGCTGCCA GTATGTTACTGAGAAGGTCCTGGCGGCTGTCTACAAGGCTCTGAGCGACCACCATGTCTATCTGGAAGG CACATTGCTGAAGCCCAACATGGTCACCCCTGGCCATGCTTGCACCCAGAAATTTTCCAATGAGGAGAT TGCCATGGCAACGGTCACAGCACTTCGTCGCACAGTGCCCCCTGCTGTCACTGGGGTCACTTTCCTGTC TGGAGGGCAGAGTGAGGAAGAGGCATCCATCAACCTCAATGCTATCAACAAGTGCCCCCTGCTGAAGCC ATGGGCCTTGACTTTCTCCTATGGTCGAGCCCTGCAGGCCTCTGCTCTAAAGGCCTGGGGTGGGAAGAA GGAGAACCTGAAGGCAGCCCAGGAGGAGTACATCAAGCGCGCCCTGGCCAACAGCCTCGCTTGTCAAGG AAAGTATACCCCAAGTGGCCAGTCTGGAGCCGCAG**CTACCTCA**TCTCTCTTCATCTCTAACCATGCCTA C**TAA*****CCAGAGCTGAACTAAGGCTGCTCCATCA**ACACTCCA**CGCGTCTGCCTACCCACTTGCTATTG AAGAGGGGTCTTCAGGCTCTTTCCCATCACTCTTGCTGCTGCCCTCGTGTGCGGTGTTGTCTGTGAATG CTAAATCTGCCATCCCTTCCAGCCCACTGCCAATAAACAACTATTTAAGGGGGAAAAAAA
Ad-AldoA 2x -255nt	CAGCTGAATAGGCTGCGTTCTCTTGGAACGCGCAGCAGAACGAGGTTCTGGTGACCCTAGCCGCGTTCG CTCCTTAGTCCTTTCGCCTACCCACCGGCGTACCAGGCAGACCCACCCCGTCCTGTGCCAGGAAAGCAC TGCCACCGGCACC**ATG**CCCCACCCATACCCAGCACTGACC**TGA**GAGCAGAAGAAGGAGCTGTCTGACAT CGCTCACCGCATTGTGGCTCCGGGCAAGGGCATCCTGGCTGCAGATGAGTCCACCGGAAGCATTGCCAA GCGCCTGCAGTCCATTGGCACCGAGAACACCGAGGAGAACAGGCGCTTCTACCGCCAGCTGCTGCTGAC TGCAGACGACCGTGTGAATCCCTGCATTGGGGGGGTGATCCTCTTCCACGAGACACTGTACCAGAAGGC AGATGATGGACGTCCCTTCCCCCAAGTTATCAAGTCCAAGGGTGGTGTTGTGGGCATTAAGGTAGATAA GGGTGTGGTGCCCCTGGCAGGAACCAATGGCGAGACAACTACCCAGGGGCTGGATGGGCTGTCTGAACG CTGTGCCCAGTATAAGAAGGATGGAGCCGACTTTGCCAAGTGGCGCTGTGTGCTAAAGATTGGGGAACA TACTCCCTCGGCCCTGGCCATCATGGAAAATGCCAATGTTCTGGCCCGTTATGCCAGCATCTGCCAGCA GAATGGCATTGTACCCATTGTGGAGCCTGAAATTCTCCCTGATGGGGACCATGACTTGAAGCGCTGCCA GTATGTTACTGAGAAGGTCCTGGCGGCTGTCTACAAGGCTCTGAGCGACCACCATGTCTATCTGGAAGG CACATTGCTGAAGCCCAACATGGTCACCCCTGGCCATGCTTGCACCCAGAAATTTTCCAATGAGGAGAT TGCCATGGCAACGGTCACAGCACTTCGTCGCACAGTGCCCCCTGCTGTCACTGGGGTCACTTTCCTGTC TGGAGGGCAGAGTGAGGAAGAGGCATCCATCAACCTCAATGCTAT**CTACCTCA**GCCCCCTGCTGAAGCC ATGGGCCTTGACTTTCTCCTATGGTCGAGCCCTGCAGGCCTCTGCTCTAAAGGCCTGGGGTGGGAAGAA GGAGAACCTGAAGGCAGCCCAGGAGGAGTACATCAAGCGCGCCCTGGCCAACAGCCTCGCTTGTCAAGG AAAGTATACCCCAAGTGGCCAGTCTGGAGCCGCAGCCAGTGAATCTCTCTTCATCTCTAACCATGCCTA C**TAA*****CCAGAGCTGAACTAAGGCTGCTCCATCA**ACACTCCA**CGCGTCTGCCTACCCACTTGCTATTG AAGAGGGGTCTTCAGGCTCTTTCCCATCACTCTTGCTGCTGCCCTCGTGTGCGGTGTTGTCTGTGAATG CTAAATCTGCCATCCCTTCCAGCCCACTGCCAATAAACAACTATTTAAGGGGGAAAAAAA
Ad-AldoA 2x -997nt	CAGCTGAATAGGCTGCGTTCTCTTGGAACGCGCAGCAGAACGAGGTTCTGGTGACCCTAGCCGCGTTCG CTCCTTAGTCCTTTCGCCTACCCACCGGCGTACCAGGCAGACCCACCCCGTCCTGTGCCAGGAAAGCAC TGCCACCGGCACC**ATG**CCCCACCCATACCCAGCACTGACC**TGA**GAGCAGAAGAAGGAGCTGTCTGACAT CGCTCACCGCATTGTGGCTCCGGGCAAGGGCATCCTGGCTGCAGATGAGTCCACCGGAAGCA**CTACCTC** **A**CGCCTGCAGTCCATTGGCACCGAGAACACCGAGGAGAACAGGCGCTTCTACCGCCAGCTGCTGCTGAC TGCAGACGACCGTGTGAATCCCTGCATTGGGGGGGTGATCCTCTTCCACGAGACACTGTACCAGAAGGC AGATGATGGACGTCCCTTCCCCCAAGTTATCAAGTCCAAGGGTGGTGTTGTGGGCATTAAGGTAGATAA GGGTGTGGTGCCCCTGGCAGGAACCAATGGCGAGACAACTACCCAGGGGCTGGATGGGCTGTCTGAACG CTGTGCCCAGTATAAGAAGGATGGAGCCGACTTTGCCAAGTGGCGCTGTGTGCTAAAGATTGGGGAACA TACTCCCTCGGCCCTGGCCATCATGGAAAATGCCAATGTTCTGGCCCGTTATGCCAGCATCTGCCAGCA GAATGGCATTGTACCCATTGTGGAGCCTGAAATTCTCCCTGATGGGGACCATGACTTGAAGCGCTGCCA GTATGTTACTGAGAAGGTCCTGGCGGCTGTCTACAAGGCTCTGAGCGACCACCATGTCTATCTGGAAGG CACATTGCTGAAGCCCAACATGGTCACCCCTGGCCATGCTTGCACCCAGAAATTTTCCAATGAGGAGAT TGCCATGGCAACGGTCACAGCACTTCGTCGCACAGTGCCCCCTGCTGTCACTGGGGTCACTTTCCTGTC TGGAGGGCAGAGTGAGGAAGAGGCATCCATCAACCTCAATGCTATCAACAAGTGCCCCCTGCTGAAGCC ATGGGCCTTGACTTTCTCCTATGGTCGAGCCCTGCAGGCCTCTGCTCTAAAGGCCTGGGGTGGGAAGAA GGAGAACCTGAAGGCAGCCCAGGAGGAGTACATCAAGCGCGCCCTGGCCAACAGCCTCGCTTGTCAAGG AAAGTATACCCCAAGTGGCCAGTCTGGAGCCGCAGCCAGTGAATCTCTCTTCATCTCTAACCATGCCTA C**TAA*****CCAGAGCTGAACTAAGGCTGCTCCATCA**ACACTCCA**CGCGTCTGCCTACCCACTTGCTATTG AAGAGGGGTCTTCAGGCTCTTTCCCATCACTCTTGCTGCTGCCCTCGTGTGCGGTGTTGTCTGTGAATG CTAAATCTGCCATCCCTTCCAGCCCACTGCCAATAAACAACTATTTAAGGGGGAAAAAAA

EXTENDED EXPERIMENTAL PROCEDURES

Fluorescent Reporter Plasmids

The reporter plasmids are based on the pTRE-Tight-BI (Clontech) and rtTA plasmid system, where a bidirectional Tet promoter expresses enhanced yellow fluorescent protein (eYFP) and mCherry (pTRE-Tight-BI mCherry/eYFP) that contain a nuclear localization signal (Mukherji et al., 2011). The 3′ UTR of *mCherry* contains either zero (0s), one (1s), or three consecutive (3s) 48 nucleotide-long-sequence stretches, which are comprised of one 8mer miRNA recognition element (MRE) and ±20 bp flanking regions (MRE-reporter-sequence). The flanking regions originate from sequences 20 bp up- and down-stream of the 8mer seed match of miR-293 in the mouse *Sirt7* 3′ UTR region(Bosson et al., 2014). rtTA, pWhitescript , pTRE-Tight-BI mCherry/eYFP 0s and three 3s reporter plasmids (for miR-293, mir-294 and miR-92) were attained from the Philipp Sharp laboratory. Reporter plasmids for miR-293 (1s), miR-294 (1s), miR-92 (1s), miR-16 (3s), miR-26 (3s) and miR-292-5p (3s) were created by cloning either one or three MRE-reporter-sequence(s) into pTRE-Tight-BI mCherry/eYFP 0s using the restriction sites HindIII and SalI (NEB) (Bosson et al., 2014). All reporter plasmid sequences were confirmed by Sanger sequencing.

Embryonic Stem Cell Culturing and Transfection

The male embryonic stem cell line E14 (from Prof. Constance Ciaudo laboratory) derived from 129/Ola mice was cultured in ESC media [DMEM 4.5 g/l glucose (Life Technologies), containing 15% heat-inactivated fetal bovine serum (Life Technologies), 1000 U/ml recombinant mouse LIF (Amsbio), 0.1 mM 2-mercaptoethanol (Sigma), 1% Penicillin-Streptomycin (Life Technologies), 1% Glutamax (Life Technologies), and 1mM sodium pyruvate (Life Technologies)] on a 0.1% gelatin-coated plated in the absence of feeder cells. For transfection, plates with ~80% confluence were trypsinized and plated at 2 x 10^5 cells/well in gelatin-coated Nucleon Delta Surface 12-well plates (Thermo Scientific). 16 to 24 hours after plating, cells were transfected in Opti-MEM (Life Technologies) with 5 μl Lipofectamine 2000 (Life Technologies), together with 250 ng reporter plasmid, 250 ng rtTA plasmid, 1000 ng pWhitescript, and when applicable with miRNA mimics (Microsynth) or Antagomir-293 (Axolabs). Six hours after transfection the media was changed to ESC media containing 1ug/ml Doxycycline (Sigma), incubated for 18 hours, and then harvested for downstream flow cytometry analysis. All cells were incubated at 37°C in a humidified atmosphere containing 5% CO_2.

Flow Cytometry

E14 were transfected with reporter and rtTA plasmids and induced with doxycycline 6 hours post-transfection as described above. 24 hours after doxycycline induction cells were trypsinized (Life Technologies) for 60–75 seconds, neutralized with ESC media, spun down for 3 min with 200g at 4°C, washed once with 1 ml ice cold FACS buffer [PBS (Life Technologies) with 5% heat-inactivated fetal bovine serum (Life Technologies)], resuspended in 100-200ul FACS buffer and kept on ice for no longer than 4 hours. Just before analysis cells were passed through a 35 μm cell strainer (Corning). Samples were analyzed by counting 100,000 events per biological replica using a FACSAria IIIu flow cytometer (BD Biosciences) and an 85 μm nozzle. For sorting, 40,000 – 75,000 cells from 3 different gates (shown in Figure S1A) were collected simultaneously into three different 1.5 ml tubes and lysed with 1 ml peqGold TriFast immediately after the completion of the sort. Flowjo software version 10 was used to extract fluorescent values of eYFP and mCherry for each cell. eYFP and mCherry fluorescent values were corrected for autofluorescence by subtracting the mean background fluorescence plus two standard deviation from mock-transfected controls as described in Bosson et al. (2014). While subtracting only the mean background fluorescence would more correctly maintain the linear relationship between the fluorescence values of the two reporters at low levels of expression, we perform this background subtraction as described to maintain consistency with prior work. We have performed our analysis by subtracting either the mean (~28 for mCherry and ~18 for eYFP), or the mean plus two standard deviations (~200 for mCherry and ~180 for eYFP), and found no large difference between the curves generated nor our resulting interpretation. Cells with fluorescence values below 0 after background subtraction were excluded from further analyses. Data were log-transformed, divided into 20 bins based on eYFP level in the range of 10^3 – 1.25 x 10^5, and mean mCherry fluorescence values were calculated for each eYFP bin. For fold-change calculations all 3s reporter co-transfections have been normalized to the 0s control with the same respective Antagomir or miRNA concentration, but only one representative 0s control is shown in the Figures. Only fold-change values with mean mCherry expression above 0.8 x 10^3 are shown in Figures 1 and 2.

Animal Experiments

Animals were maintained on a 12-hour light/dark cycle under a controlled environment in a pathogen-free facility at the Institute for Molecular Systems Biology, ETH Zürich (Switzerland). All animal experiments were approved by the ethics committee of the Kantonale Veterinäramt Zürich.

Hepatocytes Isolation, Viral Infections and Transfections

All hepatocyte experiments were performed in primary cells derived from mouse livers. Hepatocyte isolation is based on the method described by Zhang et al. (2012) with modifications described in Denzler et al. (2014). Male 8- to 12-week-old C57BL/6N mice (Janvier) were anesthetized by intraperitoneal injection of 150 μl pentobarbital (Esconarkon US vet) pre-diluted 1:5 in PBS. The liver was perfused by cannulation of the caudal vena cava with the portal vein as a drain. The liver was perfused with pre-warmed Hank's Balanced Salt Solution (Life Technologies) containing 0.5 mM EGTA followed by pre-warmed digestion medium [DMEM 1 g/l glucose (Life Technologies) supplemented with 1% Penicillin-Streptomycin (Life Technologies), 15mM HEPES (Life Technologies) and 30 μg/ml Liberase TM Research Grade medium Thermolysin concentration (Roche)] each for four minutes with a flow rate of 3 ml min^{-1}. The liver was surgically removed, hepatocytes released into 10 ml digestion media by shaking and supplemented with 15 ml ice cold low glucose media [DMEM 1 g/l glucose (Life Technologies) supplemented with 1% Penicillin-Streptomycin (Life Technologies), 10% heat-inactivated fetal bovine serum (Sigma) and 1% Glutamax (Life Technologies)] and filtered through a 100 μm Cell Strainer (BD). The suspension was then washed three times with 25 ml of ice-cold low glucose media (50 g at 4°C for 2 min). Hepatocytes were counted and plated at 300,000 cells/well in surface-treated 6-well plates (Corning Primaria) in low glucose media. 4–6 hours after plating, cells were transfected with miRNA mimics (Microsynth) employing RNAiMAX (Life Technologies) or infected with adenovirus constructs in Hepatozyme media [HepatoZYME-SFM (Life Technologies) supplemented with 1% Penicillin-Streptomycin (Life Technologies), 1% Glutamax (Life Technologies)] and harvested 24 hours post infection. All cells were incubated at 37°C in a humidified atmosphere containing 5% CO_2.

miRNA Mimics and Antagomir-293

miRNA mimics and respective negative controls were synthesized by Microsynth with dTdT overhangs in the 3' end of the sense and antisense strand. The siRNA negative control is a pool of four oligonucleotide sequences (See Table S4). Antagomir-293 was ordered from Axolabs based on the following sequence/chemistry: ascsAfscsusascsAfsasascsuscsUfsgscsgsgscsascsu (2'-O-methyl-nucleotide: a, c, g, u; 2'-fluoro-nucleotide: Af, Cf, Gf, Uf; phosphorothionate: s)

Generation of Adenovirus Constructs

Recombinant adenoviruses generated in this study are either based on the *AldolaseA*-expressing adenovirus constructs (Ad-AldoA), described in Denzler et al. (2014), harboring either one (1s) or a mutated (Mut) miR-122 binding site, or express a miRNA precursor as described in Krützfeldt et al. (2005) and Krützfeldt et al. (2012). All adenoviruses were produced by Viraquest Inc., USA, employing the plasmid pVQAd CMV K-NpA. AldolaseA variant 2 (*AldoA*, NM_007438) with a translational stop codon at amino acid residue ten and a MluI restriction site after the endogenous (1s) or mutated (Mut) miR-122 binding site was introduced into pVQAd using the restriction sites BamHI and XhoI (NEB). All adenovirus constructs express green fluorescent protein (GFP) mRNA from an independent promoter. Nucleotide sequences of all Ad-AldoA constructs used in this study were confirmed by Sanger sequencing and are shown in Tables S5 and S6.

RNA Isolation

RNA was extracted using TRI Reagent (Sigma) or peqGold TriFast (Peqlab) according to the manufacturer's instructions, except for a 30 min isopropanol precipitation at –20°C.

RNA Amounts Per Cell

To determine per cell RNA amounts for ESCs, a confluent plate was trypsinized, the cells counted and 2 x 10^5 or 2 x 10^6 cells lysed in quadruplicates in 1 ml peqGold TriFast. Dividing the recovered RNA by the number of counted cells yielded 22.95 ± 0.25 pg/cell for ESCs. RNA measurements were transformed to per cell units either with 22.95 pg/cell for ESCs or with the previously published value of 73.5/cell for primary hepatocytes (Denzler et al., 2014).

Gene Expression Analysis

2 ug of total RNA was treated with the DNA-free Kit (Life Technologies) and reverse-transcribed using the High Capacity cDNA Reverse Transcription Kit (Life Technologies). Quantitative PCR reactions were performed with the Light Cycler 480 (Roche) employing a 384-well format, gene-specific primer pairs (see Table S4, designed by http://qpcr.probefinder.com/organism.jsp) and KAPA SYBR Fast qPCR Master Mix (2x) for LightCycler 480 (Kapa Biosystems). Cycles were quantified employing Light Cycler 480 Analysis Software (Abs quantification/ 2nd derivate max). Relative gene expression was calculated using the ddCT method and mouse *36b4* (*Rplp0*) for normalization. For absolute mRNA quantification of *AldoA*, *Crot* and

ApoM standard curves from Denzler et al. (2014) were taken, where plasmids were in vitro transcribed, reverse transcribed and used for a standard curve. For absolute quantification of *eYFP* and *mCherry*, a dilution series of *eYFP*, *mCherry* and containing plasmids were directly used in qPCR reactions to create standard curves, as *AldoA* standard curves derived directly from plasmids were similar that those retained through in vitro transcription. Molar concentrations of plasmids were quantified using a NanoDrop ND-1000 spectrophotometer (Thermo Scientific) and the respective molecular weight.

miRNA Expression Analysis

miRNA expression analysis was performed as previously described in Denzler et al. (2014). 240 ng of total RNA was reverse-transcribed using TaqMan MicroRNA Assays (Life Technologies) and TaqMan MicroRNA Reverse Transcription Kit (Life Technologies). The RT primers were multiplexed in a dilution of 1:20 as described by the manufacturer. To avoid quantification biases caused by similar miRNA sequences, miRNAs of the same seed family were not multiplexed in the same reaction. Quantitative PCR reactions were performed with the Light Cycler 480 (Roche) employing a 384-well format, TaqMan Universal PCR Master Mix, No AmpErase UNG (Life Technologies) and TaqMan MicroRNA Assays (Life Technologies). Cycles were quantified employing Light Cycler 480 analysis software (Abs quantification/ 2^{nd} derivate max). Relative miRNA expression was calculated using the ddCT method and mouse snoRNA202 for normalization. For absolute quantification synthetic miRNAs (Sigma-Aldrich) were quantified using a NanoDrop ND-1000 spectrophotometer (Thermo Scientific) and the respective molecular weight. miRNAs were spiked into primary hepatocyte cell lysates and absolutely quantified employing a synthetic miRNA standard curve. Absolute miRNA copy numbers of adenovirus-infected primary hepatocytes shown Figures S3A and S4M were calculated by multiplying relative abundances (miRNA/snoRNA202), which were normalized to uninfected hepatocytes, with the copy number evaluated in either Figure 4A or in Denzler et al. (2014)

Small RNA Sequencing and Data Analysis:

Total RNA was size fractionated (18–35 nt), followed by 5’ adapter (Truseq small RNA 5’ adapter RA5 + 8Ns, GUUCAGAGUUCUACAGUCCGACGAUCNNNNNNNN) and 3’ adapter (NNNNAGAUCGGAAGAGCACACGUCU/3ddC/) ligations, RT-PCR, and Solexa sequencing. To quantify miRNA levels, we counted the number of occurrences in which the first 20 nt of the raw sequence matched a known mature

Mus musculus miRNA sequence of miRBase version 20. All raw and processed data files have been deposited in GEO and can be found under the accession number GSE76288.

RNA-seq Data Analysis

To process RNA-seq data, we utilized the same general strategy described previously (Denzler et al., 2014). Briefly, raw reads were aligned to the latest build of the mouse genome (mm10) using STAR v. 2.3.1n (options --outFilterType BySJout --outFilterMultimapScoreRange 0 --readMatesLengthsIn Equal --outFilterIntronMotifs RemoveNoncanonicalUnannotated --clip3pAdapterSeq TCGTATGCCGTCTTCTGCTTG --outStd SAM (Dobin et al., 2013). Pooling all biological replicates of a particular sample, differential expression analysis was performed between two samples of interest using cuffdiff v. 2.1.1 (options --library-type fr-firststrand -b mm10.fa -u --max-bundle-frags 100000000) (Trapnell et al., 2013), using mouse transcript models of protein-coding and long noncoding RNA genes annotated in Ensembl release 72. All raw and processed data files have been deposited in GEO and can be found under the accession number GSE76288. For data analysis, only genes with FPKM above 2.0 (ESCs) or above 1.0 (primary hepatocytes) were considered. For cumulative distribution function calculations, fold change values (log2) were corrected for biases due to 3′ UTR length by fitting a linear model to mRNA fold change (log2) as a function of the 3′ UTR length of each respective transcript (see Tables S1 and S3), and subsequently subtracting the predicted model value for all transcripts.

Absolute Copy Numbers Evaluation from RNA-seq Data (ESCs)

We fit a linear regression function to transform gene expression measurements (measured in FPKM) from RNA-seq data into absolute copy numbers (as determined by quantitative PCR). The data was log-transformed and fit to a linear equation of the form Y = X + B, in which Y = log(y) and X = log(x). Fixing the slope to be 1 constrains the regression such that a linear relationship is maintained between the non-transformed values, x and y. Copy numbers per cell were determined by multiplying the FPKM by 10^B, in which B is the y-intercept from the fit linear regression. To transform published ESC RNA-seq data (Bosson et al., 2014) we fit a linear regression between log-transformed FPKM of published ESC data and FPKM from ESCs transfected with the 0s reporter and sorted for low eYFP expressing cells, with the same equation as above. Copy numbers per cell were then determined by multiplying the FPKM of published ESC data by the transformed y-intercept, 10^B.

Absolute Copy Number Evaluation from RNA-seq Data (Primary Hepatocytes)

To transform our primary hepatocyte data from this study to copies per cells we fit a linear regression function between log-transformed FPKM of published hepatocytes (Denzler et al., 2014), where copy numbers of sequencing data were known, and FPKM of primary hepatocytes from this study, with the same equation as described in the previous paragraph. Copy numbers per cell were then determined by multiplying the FPKM of published hepatocyte data by the transformed y-intercept, 10^B.

Small RNA Sequencing and Data Analysis:

Total RNA was size fractionated (18–35 nt), followed by ligation of 3' preadenylated adapter (AppNNNNAGATCGGAAGAGCACACGTCTddC) and 5' adapter (Truseq small RNA 5' adapter RA5 + 8Ns, GUUCAGAGUUCUACAGUCCGACGAUCNNNNNNNN), reverse transcription, PCR amplification, and Solexa sequencing. To quantify miRNA levels, we counted the number of occurrences in which the first 20 nt of the raw sequence matched a known mature Mus musculus miRNA sequence of miRBase version 20. All raw and processed data files have been deposited in GEO and can be found under the accession number GSE76288.

Target Abundance Calculation

For each miRNA, the copy number of each predicted target gene was multiplied with the number of 6-, 7-, and 8-nt 3′ UTR binding sites, and these values were summed to yield TA_{app}.

Northern Blotting

Northern blotting was performed as described in Title et al. (2015). 10 ug of RNA, were denatured and separated on a 15% denaturing polyacrylamide gel containing 7.5 M urea (SequaGel, National Diagnostics). Separated RNAs were then transferred onto a Hybond Nx nylon membrane (GE Healthcare Life Sciences) and cross-linked using 1-ethyl-3-(3-dimethylaminopropyl) carbodiimide (Thermo Scientific) as detailed by Pall and Hamilton (2008). miR-122 and miR-16 DNA oligonucleotide probes were designed as the reverse complement of the mature miRNA sequence or the U6 transcript (See Table S4). 20 pmol was labeled with [γ-^{32}P]dATP (PerkinElmer Life Sciences) using T4 polynucleotide kinase (NEB). Membranes were prehybridized at 50 °C under rotation for 1 h and hybridized with the labeled probe overnight (20 mM Na_2HPO_4 (pH 7.2), 7% SDS, 25% 20x SSC, 0.02% albumin, 0.02% polyvinyl-

pyrrolidon K30, 0.02% Ficoll 400, and 0.1 mg/ml sonicated salmon sperm), followed by washing twice with buffer 1 (25% 20x SSC, and 5% SDS) and once with buffer 2 (5% 20x SSC, and 1% SDS) and exposure to a phosphorimaging screen for 8 hours to O/N. Signal was detected using the FLA-7000 (FujiFilm). Membranes were stripped with boiled 0.1% SDS, shaking, twice for 20 minutes, and exposed for a minimum of 24 hours to verify loss of signal.

Calculation of IC_{50} values from dual-reporter experiments

To determine the abundance of competing sites at which the amount of miRNA-mediated repression has decreased to half of that observed in the absence of competing sites, IC_{50}, the 3s reporter data were fit to a modified Hill equation using non-linear least-squares. The following describes how this equation was generated, as well as the relationship between maximal and half-maximal miRNA-mediated repression.

The time evolution of the cellular abundance of an mRNA *x* can be described as

$$\frac{dx}{dt} = \alpha - \beta x \qquad [1.1]$$

where α is the rate of transcription, and β is the first-order rate constant for its degradation. We highlight that the β term is a simplification representing an average over a variety of states of the mRNA and corresponding degradation rates. To highlight this we refer to β as β_{app}.

By setting the left-hand-side of equation [1.1] to 0, we arrive at expressions for the steady-state abundance of both a site-containing mRNA *s* and the corresponding no-site containing mRNA s_0

$$s = \frac{\alpha}{\beta_{app}} \ , \qquad [1.2]$$

$$s_0 = \frac{\alpha}{\beta_{0,app}} \ . \qquad [1.3]$$

We make the assumption that miRNA effects do not interfere with the miRNA-independent degradation mechanisms represented by $\beta_{0,app}$, allowing us to write equation [1.2] as

$$s = \frac{\alpha}{\beta_{0,app} + \beta_{miR,app}} \ . \qquad [1.4]$$

Where $\beta_{miR,app}$ is the apparent rate constant for miRNA-mediated degradation.

The observed fractional repression ρ is therefore given by

$$\rho = \frac{s}{s_0} = \frac{1}{1+R} \ , \qquad [1.5]$$

where $R = \beta_{miR,app}/\beta_{0,app}$, and represents the normalized increase in degradation of *s* due to miRNA-mediated repression. In the regime of target-site excess, the effects of the miRNA will be distributed equally across the entire pool of target sites, and so *R* will scale inversely with the target site abundance (TA):

$$R \propto \frac{1}{\mathrm{TA}} \ . \qquad [1.6]$$

Therefore, in conditions of constant miRNA concentration, the value of *R* with added competitor abundance s_e is given by

$$R = R_0 \frac{\mathrm{TA}}{s_e + \mathrm{TA}} \ , \qquad [1.7]$$

where R_0 is the value of *R* in the absence of added competitor.

For the dual reporter experiments, we use a modified version of this equation accounting for a three-site containing reporter with cooperative spacing:

$$R_{3site} = R_0 \frac{\mathrm{TA}^n}{(3s_e)^n + \mathrm{TA}^n} \qquad [1.8]$$

where *n* is the Hill coefficient for cooperative binding. Substituting *R* from equation [1.8] into [1.5] and rearranging yields

$$\rho = \frac{(3s_e)^n + \mathrm{TA}^n}{(3s_e)^n + \mathrm{TA}^n(1+R_0)} \ , \qquad [1.9]$$

which was fit against the data of Figures 1, 2, and S2.

Setting $s_e = 0$ in equation [1.9] to generate ρ_0, the value of ρ in the absence of added competitor, and rearranging yields

$$R_0 = \frac{1-\rho_0}{\rho_0} \ . \qquad [1.10]$$

Half-maximal derepression ρ_{50} is given by setting $R = R_0/2$ in equation [1.5] and substituting R_0 from equation [1.10]

$$\rho_{50} = \frac{1}{1+\frac{1}{2}R_0} = \frac{2\rho_0}{\rho_0+1} \ . \qquad [1.11]$$

This relationship is also used to calculate IC_{50} values in mathematical simulations of miRNA competition.

For the dual-reporter experiments measuring *mCherry* derepression in ESCs, the depression threshold (DRT) was defined as the abundance of competing target at which the fractional repression is equal to 90% of its maximum:

$$\rho_{\mathrm{DRT}} = \left(\rho_0\right)^{9/10} \qquad [1.12]$$

For the qPCR experiments measuring endogenous miRNA target derepression in primary hepatocytes, we used a variant of equation [1.9] normalized to ρ_0

$$\rho_{\text{norm}} = \frac{\rho}{\rho_0} = 1 + \frac{(3s_e)^n R_0}{(3s_e)^n + \text{TA}^n\left(1 + R_0\right)} \ , \qquad [1.13]$$

which was fit against the data of Figure S7 for the AldoA 3-site construct. In case of data originating from 1-site AldoA constructs in Figures 3, 4, 5, and 6, equation [1.13] was used in which n was set to 1 and $3s_e$ was replaced with s_e. In addition, since the number of added *AldoA* MREs never reached a level sufficient to observe complete derepression, the R_0 parameter from equation [1.13] could not accurately be fit. This precludes the DRT calculation as performed with the dual reporter experiments. We therefore modified our definition of DRT for the qPCR experiments to represent the abundance of competing target at which endogenous target genes have been upregulated by 10%.

$$\rho_{\text{DRT}_{\text{qPCR}}} = 1.1 \qquad [1.14]$$

Due to the measurement noise associated with the derepression signal for weak targets, the DRT was calculated by the average DRT of the two genes exhibiting the largest derepression.

Mathematical modeling of miRNA-mediated repression

As done previously (Mukherji et al., 2011; Ala et al., 2013; Bosson et al., 2014; Jens and Rajewsky, 2015; Schmiedel et al., 2015), we constructed a system of differential equations describing the regulation of mRNA targets by a miRNA. The system was solved at steady-state to arrive at an equation relating the occupancy and repression of each mRNA to the abundance and binding affinity of each mRNA, as well as the activity and abundance of the miRNA. The model includes a miRNA-programmed silencing complex (hereafter referred to as "free miRNA") m, and an arbitrary number of distinct mRNA target site types (hereafter referred to as "sites") $\boldsymbol{s} = (s_1, s_2, \ldots, s_n)$. The free miRNA can reversibly bind each free site s_i to form the corresponding miRNA–site complex (hereafter referred to as "complex") c_i. The mRNA species belonging to c_i is then subject to increased (miRNA-mediated) degradation. The behavior of this model is described by a system of coupled first-order differential equations, where:

$$\frac{dm}{dt} = \alpha_m - \beta_m m + \sum_i \left[\left(\beta_c + \beta_i + k_i^- \right) c_i - k_i^+ s_i m \right] \ , \qquad [2.1]$$

and for each site–complex pair:

$$\frac{ds_i}{dt} = \alpha_i + \left(\beta_m + k_i^-\right)c_i - \left(\beta_i + k_i^+ m\right)s_i \ , \qquad [2.2]$$

$$\frac{dc_i}{dt} = k_i^+ m s_i - \left(\beta_i + \beta_m + \beta_c + k_i^-\right)c_i \ . \qquad [2.3]$$

Free miRNA *m* is generated at rate α_m and degraded due to dilution and decay with rate constant β_m. Similarly, each site s_i is generated at rate α_i and degraded with rate constant β_i. Each complex c_i is formed from the association of free miRNA *m* and site s_i with rate constant k_i^+, and is lost due to either complex dissociation with rate constant k_i^-, independent degradation of either the miRNA or the mRNA within the complex with rate constant β_i or β_m respectively, or miRNA-dependent degradation of the mRNA within the complex with rate constant β_c. Independent degradation of the miRNA within the complex regenerates the free site s_i, whereas independent or miRNA-dependent degradation of the mRNA within the complex regenerates the free miRNA *m.*

Setting the left-hand side of equations [2.2] and [2.3] to 0 yields the steady-state solutions for s_i and c_i

$$s_i = \frac{\alpha_i K_i}{\beta_i\left(K_i + mB_i\right)} \ , \qquad [2.4]$$

$$c_i = \frac{\alpha_i m}{\beta_i\left(K_i + mB_i\right)} \ , \qquad [2.5]$$

where

$$B_i = \frac{\beta_i + \beta_c}{\beta_i} \ , \qquad [2.6]$$

is the maximum miRNA activity, or the fold-difference in stability between the free and bound form of each site *i* due to repression, and

$$K_i = \frac{\beta_c + \beta_i + \beta_m + k_i^-}{k_i^+} \ , \qquad [2.7]$$

is the Michaelis constant giving the concentration of the free site s_i at which repression will be half that of the maximum miRNA activity. This is distinct from the experimentally determined IC_{50} value, which reports the amount of additional competing sites necessary to observe half the repression of a miRNA target site compared to the condition in which no competing sites are added.

Substituting equations [2.4] and [2.5] into equation [2.1] and setting the left-hand side to 0 rearranges to an implicit expression for the steady-state solution for *m*:

$$\frac{\alpha_m}{\beta_m} = m + \frac{1}{\beta_m}\sum_i \left[\frac{m\left(K_i k_i^+ - k_i^- - \beta_i - \beta_c\right)}{K_i + mB_i} \frac{\alpha_i}{\beta_i} \right] . \quad [2.8]$$

By first rearranging equation [2.7] to

$$K_i k_i^+ = k_i^- + \beta_i + \beta_c + \beta_m \ , \quad [2.9]$$

and using equation [2.9] to substitute for $K_i k_i^+$, equation [2.8], can be simplified to

$$M = m + \sum_i \frac{m}{K_i + mB_i} T_i \ , \quad [2.10]$$

where $M = \alpha_m / \beta_m$ is the total amount of miRNA in the system, and $T_i = \alpha_i / \beta_i$ is the total amount of site *i* in the absence of repression. The fractional occupancy θ_i and the fractional repression ρ_i of each site *i* are given by

$$\theta_i \equiv \frac{c_i}{c_i + s_i} = \frac{m}{m + K_i} \ , \quad [2.11]$$

$$\rho_i \equiv \frac{c_i + s_i}{T_i} = \frac{K_i + m}{K_i + mB_i} \ , \quad [2.12]$$

which allow equation [2.10] to be written as

$$M = m + \sum_i \theta_i \rho_i T_i \ , \quad [2.13]$$

or two alternative forms

$$M = m + \sum_i \theta_i T_i' \ , \quad [2.14]$$

where $T_i' = \rho_i T_i$ represents the total amount of site *i* (incorporating repression) and

$$M = m + \sum_i c_i \ , \quad [2.15]$$

which recovers the definition of total miRNA *M* as the sum of free miRNA *m* and all complexes c_i in which it is engaged.

We applied two simplifications to the model, for the ease of implementation. First, we assigned a single value of *B* to all sites within a particular simulation. While the value of B_i is expected to vary across genes inversely related to mRNA half-life, the occurrences of each site are spread over many distinct mRNA species, allowing reasonable approximation of maximal miRNA activity in a particular cell type by a single parameter value. Second, we approximated the Michaelis terms as:

$$K_i \approx \frac{k_i^-}{k_i^+} = K_{\mathrm{D},i} \ , \quad [2.16]$$

given that reported rates of complex dissociation for high-affinity sites (Salomon et al., 2015) vastly exceed decay rates inferred from median mRNA half-life (9 h) (Schwanhausser et al., 2011). With these two adjustments, the final form of the

modeled system in equation [2.13] is parameterized by the abundances of each molecular species, in addition to two steady-state parameters B and $K_{D,i}$. This had the advantage of being immediately applicable to the dual fluorescence experiments, for which rate constants are not directly known.

We simulated either the occupancy or repression of an arbitrary site j (with dissociation constant $K_{D,j}$) in the presence of a competitor site e (with abundance T_e' that was varied across simulations and dissociation constant $K_{D,e}$) in addition to the pool of endogenous sites $\boldsymbol{s}$ (each with known, invariant abundance T_i' and dissociation constant $K_{D,i}$) and a given value of maximal miRNA activity B by application of either equation [2.11],

$$\theta_j = \frac{m_e}{K_{D,j} + m_e} \qquad [2.17]$$

or equation [2.12]:

$$\rho_j = \frac{K_{D,j} + m_e}{K_{D,j} + m_e B} \qquad [2.18]$$

where m_e is determined by solving equation [2.13] updated to include site e:

$$M = m_e + \sum_i \frac{m_e}{K_{D,i} + m_e B} T_i + \frac{m_e}{K_{D,e} + m_e} T_e' \ , \qquad [2.19]$$

in which the values of T_i are found by rearranging equation [2.12]:

$$T_i = \rho_i^{-1} T_i' = \frac{m_0 B + K_{D,i}}{m_0 + K_{D,i}} T_i' \ , \qquad [2.20]$$

where m_0 is the abundance of free miRNA in the absence of competitor, found by solving equation [2.15] in the absence of site e:

$$M = m_0 + \sum_i \frac{m_0}{K_{D,i} + m_0} T_i' \ . \qquad [2.21]$$

When simulating the mixed-affinity model for miR-293 in ESCs, we assigned parameter values as follows:

1.) M was set to the cellular miRNA abundance (2.6×10^3 copies per cell, or cpc).

2.) B was set according to 3.9, based on the amount of repression observed for an 8-nt site in the absence of added sites (~20%).

3.) The paired values for site abundances (T'_1, T'_2, …, T'_n) and dissociation constants ($K_{D,1}$, $K_{D,2}$, …, $K_{D,n}$) were determined through a two-step procedure. In the first step, we first generated T' and K_D values representing four distinct site type categories (8-, 7-, 6-nt and low-affinity sites). We set the total number of 8-, 7-, and 6-nt sites T'_{8nt}, T'_{7nt}, and T'_{6nt} by taking the number of canonical 3′ UTR sites in the absence of added exogenous target (2.1×10^4 cpc) and apportioning them at a 1:6:9

ratio. The representative dissociation constant for the 8-nt site $K_{D,8nt}$ was drawn from single-molecule experiments (18 pM) (Salomon et al., 2015), with the $K_{D,7nt}$ and $K_{D,6nt}$ scaled by 2- and 5-fold, respectively, based on the relative efficacy of either site in competition (Figure 5). We modeled the contribution of low-affinity sites, i.e., noncanonical/background sites, by assigning the fourth site type a representative dissociation constant $K_{D,la}$ arbitrarily scaled 300-fold in comparison to the 8-nt site, and setting the abundance of this site type T'_{la} such that the simulated IC_{50} (the combined effect of all four endogenous site types) agreed with experimental observation (3.3 x 10^4 cpc). The four representative K_D values were converted from pM to cpc based on a cellular diameter of 10 μm (Hong et al., 2012) and a cytoplasmic volume of 40% (Bosson et al., 2014). In the second step, we generated 10^3, 10^3, 10^3, and 10^4 variants of each the four site types, respectively. Each site-type variant was assigned a dissociation constant $K_{D,i}$ by log-transforming a value sampled from a normal distribution with mean = exp(K_D) and standard deviation = 0.3 x exp(K_D), where K_D is set to the corresponding value from the first step ($K_{D,8nt}$, $K_{D,7nt}$, $K_{D,6nt}$, or $K_{D,la}$). The T'_i value for each site type variant was set to the corresponding T' value from the first step (T'_{8nt}, T'_{7nt}, and T'_{6nt}, or T'_{la}) divided by the number of variants generated for that site type. We note that the aggregate effect of the low-affinity sites could be modeled without knowing the precise affinities and abundances of these sites because choosing different affinities would have caused corresponding adjustments to the inferred abundances to reach the same effect. Therefore, although the abundances and affinities of these low-affinity sites were unknown, their influence on the experimentally determined IC_{50} values, and thus their aggregate contribution to effective target abundance, was robustly simulated.

All simulations were performed using R to solve for *m* for a range of concentrations of the competing target (1 x 10^2 – 1 x 10^5 cpc). Repression of *mCherry* as a function of *mCherry* (Figure 7A, left) or *eYFP* (Figure 7A, middle) abundance is shown by plotting ρ_j from equation [2.18] as a function of either T_j or T'_j, respectively. The fraction of *mCherry* unbound to miRNA as a function of *mCherry* abundance (Figure 7B) is given by 1 – θ_j from equation [2.17] as a function of T'_j. The model from Bosson et al. (Figure 7C, left) was implemented as previously described (Bosson et al., 2014) and the model from Jens & Rajewsky (Figure 7C, right) was adapted by multiplying each $K_{D,i}$ by R_{vol}, the ratio of cytoplasmic volume of ESCs to that of monocytes, and multiplying each T'_i by R_{TA}, the ratio of the TA_{app} value for miR-293 ESCs to that of miR-20a in monocytes. To observe these models with added low-affinity sites (Figure 7D), we added 10^4 site types, assigning each a $K_{D,i}$ value by log-

transforming a value sampled from a normal distribution with mean = exp(300 x $K_{D,8nt\ site}$) and standard deviation = 0.3 x exp(300 x $K_{D,8nt\ site}$). The abundance of each of the 10^4 sub-types was chosen such that the combined effect of these new sites and those originally present in either model resulted in an IC_{50} in agreement with experimental observation (3.3 x 10^4 cpc).

The IC_{50} for site occupancy (represented by a solid vertical line in Figures 7B, C, and D) is given by the abundance of competing site at which the fraction of that site (and all other sites with identical K_D) that is bound by miRNA is half of that modeled in the absence of competing sites:

$$M = m_{50,\theta} + \sum_i \frac{m_{50,\theta}}{K_{D,i} + m_{50,\theta} B} T + \frac{m_{50,\theta}}{K_{D,e} + m_{50,\theta}} \mathrm{IC}_{50,\theta} \ , \qquad [2.22]$$

where $m_{50,e}$ satisfies the relationship:

$$\theta_e(m_{50,\theta}) = \frac{1}{2}\theta_e(m_0) \ , \qquad [2.23]$$

such that

$$m_{50,\theta} = \frac{K_{D,i} m_0}{m_0 + 2K_{D,i}} \ . \qquad [2.24]$$

The IC_{50} for site repression (represented by a solid vertical line in both panels of Figure 7A) is given by the abundance of competing site *e* at which the apparent rate of miRNA-mediated degradation of the target has decreased by half of that modeled in the absence of competing sites:

$$M = m_{50,\rho} + \sum_i \frac{m_{50,\rho}}{K_{D,i} + m_{50,\rho} B} T + \frac{m_{50,\rho}}{K_{D,e} + m_{50,\rho}} \mathrm{IC}_{50,\rho} \ , \qquad [2.25]$$

where $m_{50,e}$ satisfies the relationship

$$\rho_e(m_{50,\rho}) = \frac{2\rho_e(m_0)}{\rho_e(m_0)+1} \ , \qquad [2.26]$$

from equation [1.12] describing the calculation of IC_{50} from the dual-reporter experiments. This also yields

$$m_{50,\rho} = \frac{K_{D,i} m_0}{m_0 + 2K_{D,i}} \ , \qquad [2.27]$$

demonstrating that the IC_{50} for repression calculated in the previous section reports on the IC_{50} for occupancy, without directly monitoring occupancy. Indeed, equation [2.18], which describes the level of repression within the steady-state model, can be rearranged and substituted with equation [2.17] yielding an equivalent form as the empirical definition of repression expressed in equation [1.5]:

$$\rho_i = \frac{1}{1 + \theta_i \left(B_i - 1 \right)} \ , \qquad [2.28]$$

demonstrating that R from equation [1.5] is proportional to θ, and so must have equivalent half-maximal competition values.

The DRT (represented by the dashed vertical lines in the left and middle panels of Figure 7A) was defined as the abundance of competing site at which the apparent rate of miRNA-mediated degradation of the target has decreased to 90% of its maximum value on a logarithmic scale:

$$M = m_{\mathrm{DRT}} + \sum_i \frac{m_{\mathrm{DRT}}}{K_{\mathrm{D},i} + m_{\mathrm{DRT}}} T_i + \frac{m_{\mathrm{DRT}}}{K_{\mathrm{D},e} + m_{\mathrm{DRT}}} \mathrm{DRT} \ , \qquad [2.29]$$

where

$$\rho_e(m_{DRT}) = \left(\rho_e(m_0)\right)^{\frac{9}{10}} \qquad [2.30]$$

For the mixed affinity model of miR-293 in ESCs, parameter values were as follows: B = 3.9, T'_{8nt} = 1.31 x 10^3 cpc, T'_{7nt} = 7.88 x 10^3, T'_{6nt} = 1.18 x 10^4, T'_{la} = 4.12 x 10^6, $K_{D,8nt}$ = 2.27 cpc, $K_{D,7nt}$ = 4.54 cpc, $K_{D,6nt}$ = 11.3 cpc, and $K_{D,la}$ = 6.80 x 10^2 cpc, with M = 8.22 x 10^2 cpc (light blue curve), 2.60 x 10^3 cpc (blue curve), or 8.22 x 10^3 (dark blue curve), and T'_e ranging from 10^2 to 10^5 cpc. For the occupancy model adapted from Bosson et al. (2014), parameter values were as follows: T'_{la} = 5.00 x 10^6 cpc and $K_{D,la}$ = 5.83 x 10^2 cpc, with M = 8.31 x 10^2 cpc (light blue curve), 2.63 x 10^3 cpc (blue curve), or 8.31 x 10^3 (dark blue curve), and T'_e ranging from 10^2 to 10^5 cpc. For the model adapted from Jens and Rajewsky (2015), parameter values were as follows: R_{vol} = 0.188, R_{TA} = 0.139, T'_{la} = 4.10 x 10^6 cpc, and $K_{D,la}$ = 2.31 x 10^3 cpc, with M = 8.22 x 10^2 cpc (light blue curve), 2.60 x 10^3 cpc (blue curve), or 8.22 x 10^3 (dark blue curve), and T'_e ranging from 10^2 to 10^5 cpc.

SUPPLEMENTAL REFERENCES

Ala, U., Karreth, F.A., Bosia, C., Pagnani, A., Taulli, R., Leopold, V., Tay, Y., Provero, P., Zecchina, R., and Pandolfi, P.P. (2013). Integrated transcriptional and competitive endogenous RNA networks are cross-regulated in permissive molecular environments. Proc Natl Acad Sci U S A *110*, 7154-7159.

Bosson, A.D., Zamudio, J.R., and Sharp, P.A. (2014). Endogenous miRNA and target concentrations determine susceptibility to potential ceRNA competition. Mol Cell *56*, 347-359.

Denzler, R., Agarwal, V., Stefano, J., Bartel, D.P., and Stoffel, M. (2014). Assessing the ceRNA hypothesis with quantitative measurements of miRNA and target abundance. Mol Cell *54*, 766-776.

Dobin, A., Davis, C.A., Schlesinger, F., Drenkow, J., Zaleski, C., Jha, S., Batut, P., Chaisson, M., and Gingeras, T.R. (2013). STAR: ultrafast universal RNA-seq aligner. Bioinformatics *29*, 15-21.

Hong, S., Pan, Q., and Lee, L.P. (2012). Single-cell level co-culture platform for intercellular communication. Integr Biol (Camb) *4*, 374-380.

Jens, M., and Rajewsky, N. (2015). Competition between target sites of regulators shapes post-transcriptional gene regulation. Nat Rev Genet *16*, 113-126.

Krutzfeldt, J., Rajewsky, N., Braich, R., Rajeev, K.G., Tuschl, T., Manoharan, M., and Stoffel, M. (2005). Silencing of microRNAs in vivo with 'antagomirs'. Nature *438*, 685-689.

Krutzfeldt, J., Rosch, N., Hausser, J., Manoharan, M., Zavolan, M., and Stoffel, M. (2012). MicroRNA-194 is a target of transcription factor 1 (Tcf1, HNF1alpha) in adult liver and controls expression of frizzled-6. Hepatology *55*, 98-107.

Mukherji, S., Ebert, M.S., Zheng, G.X., Tsang, J.S., Sharp, P.A., and van Oudenaarden, A. (2011). MicroRNAs can generate thresholds in target gene expression. Nat Genet *43*, 854-859.

Pall, G.S., and Hamilton, A.J. (2008). Improved northern blot method for enhanced detection of small RNA. Nat Protoc *3*, 1077-1084.

Salomon, W.E., Jolly, S.M., Moore, M.J., Zamore, P.D., and Serebrov, V. (2015). Single-Molecule Imaging Reveals that Argonaute Reshapes the Binding Properties of Its Nucleic Acid Guides. Cell *162*, 84-95.

Schmiedel, J.M., Klemm, S.L., Zheng, Y., Sahay, A., Bluthgen, N., Marks, D.S., and van Oudenaarden, A. (2015). Gene expression. MicroRNA control of protein expression noise. Science *348*, 128-132.

Schwanhausser, B., Busse, D., Li, N., Dittmar, G., Schuchhardt, J., Wolf, J., Chen, W., and Selbach, M. (2011). Global quantification of mammalian gene expression control. Nature *473*, 337-342.

Title, A.C., Denzler, R., and Stoffel, M. (2015). Uptake and Function Studies of Maternal Milk-derived MicroRNAs. J Biol Chem *290*, 23680-23691.

Trapnell, C., Hendrickson, D.G., Sauvageau, M., Goff, L., Rinn, J.L., and Pachter, L. (2013). Differential analysis of gene regulation at transcript resolution with RNA-seq. Nature Biotechnology *31*, 46-+.

Zhang, W., Sargis, R.M., Volden, P.A., Carmean, C.M., Sun, X.J., and Brady, M.J. (2012). PCB 126 and other dioxin-like PCBs specifically suppress hepatic PEPCK expression via the aryl hydrocarbon receptor. PLoS One *7*, e37103.